

Deep-water sediment transport patterns and basin floor topography in early rift basins: Plio-Pleistocene syn-rift of the Corinth Rift, Greece

Martin Muravchik¹  | Gijs A. Henstra¹ | Gauti T. Eliassen¹ | Rob L. Gawthorpe¹  | Mike Leeder² | Haralambos Kranis³  | Emmanuel Skourtsos³ | Julian Andrews²

¹Department of Earth Science, University of Bergen, Bergen, Norway

²School of Environmental Sciences, University of East Anglia, Norwich, UK

³Faculty of Geology and Geoenvironment, University of Athens, Athens, Greece

Correspondence

Martin Muravchik, Department of Earth Science, University of Bergen, Bergen, Norway.

Email: martin.muravchik@uib.no

Funding information

Norges Forskningsråd, Grant/Award Number: Project 255229/E30; Research Council of Norway; University of Bergen; National and Kapodistrian University of Athens

Abstract

Our current understanding on sedimentary deep-water environments is mainly built of information obtained from tectonic settings such as passive margins and foreland basins. More observations from extensional settings are particularly needed in order to better constrain the role of active tectonics in controlling sediment pathways, depositional style and stratigraphic stacking patterns. This study focuses on the evolution of a Plio-Pleistocene deep-water sedimentary system (Rethi-Dendro Formation) and its relation to structural activity in the Amphithea fault block in the Corinth Rift, Greece. The Corinth Rift is an active extensional basin in the early stages of rift evolution, providing perfect opportunities for the study of early deep-water syn-rift deposits that are usually eroded from the rift shoulders due to erosion in mature basins like the Red Sea, North Sea and the Atlantic rifted margin. The depocentre is located at the exit of a structurally controlled sediment fairway, approximately 15 km from its main sediment source and 12 km basinwards from the basin margin coastline. Fieldwork, augmented by digital outcrop techniques (LiDAR and photogrammetry) and clast-count compositional analysis allowed identification of 16 stratigraphic units that are grouped into six types of depositional elements: A—mudstone-dominated sheets, B—conglomerate-dominated lobes, C—conglomerate channel belts and sandstone sheets, D—sandstone channel belts, E—sandstone-dominated broad shallow lobes, F—sandstone-dominated sheets with broad shallow channels. The formation represents an axial system sourced by a hinterland-fed Mavro delta, with minor contributions from a transverse system of conglomerate-dominated lobes sourced from intrabasinal highs. The results of clast compositional analysis enable precise attribution for the different sediment sources to the deep-water system and their link to other stratigraphic units in the area. Structures in the Amphithea fault block played a major role in controlling the location and orientation of sedimentary systems by modifying basin-floor gradients due to a

The peer review history for this article is available at <https://publons.com/publon/10.1111/bre.12423>

This is an open access article under the terms of the Creative Commons Attribution License, which permits use, distribution and reproduction in any medium, provided the original work is properly cited.

© 2019 The Authors. Basin Research published by International Association of sedimentologists and European Association of Geoscientists and Engineers and John Wiley & Sons Ltd

combination of hangingwall tilt, displacement of faults internal to the depocentre and folding on top of blind growing faults. Fault activity also promoted large-scale subaqueous landslides and eventual uplift of the whole fault block.

1 | INTRODUCTION

Most of the present day knowledge on sedimentary deep-water environments originates from studies located at passive margins (e.g. Wynn, Kenyon, Masson, Stow, & Weaver, 2002; Gee, Gawthorpe, Bakke, & Friedmann, 2007; Deptuck, Sylvester, Pirmez, & O'Byrne, 2007; Armitage, McHargue, Fildani, & Graham, 2012; Aspiroz-Zabala et al., 2017), foreland basins (e.g. Winn & Dott, 1979; Fildani et al., 2013; Hodgson et al., 2006; Hubbard, Romans, & Graham, 2008; Johnson, Flint, Hinds, & de Ville Wickens, H., 2001) and the offshore California strike-slip basins (e.g. Carvajal et al., 2017; Normark, 1978; Symons et al., 2017). Information obtained from extensional basins is relatively small (e.g. Ferentinos, Papatheodorou, & Collins, 1988; Henstra et al., 2016; Jackson, Larsen, Hanslien, & Tjemsland, 2011; Leeder et al., 2002; Leppard & Gawthorpe, 2006; McArthur, Kneller, Wakefield, Souza, & Kuchle, 2016; Papatheodorou & Ferentinos, 1993; Ravnås & Steel, 1997; Strachan et al., 2013; Zhang & Scholz, 2015; Zhang et al., 2014), especially on aspects like rock body geometries, sediment pathways and their interaction with evolving depocentre structures.

The compartmentalized nature of extensional basins plays a crucial role in determining the dimensions and geometry of deep-water sedimentary rock bodies as well as their orientation and stacking patterns. This is because the uplift and subsidence generated by extensional tectonics creates vertical offsets in the order of thousands of metres occurring at a fault-block scale (usually between 10 to 30 km in length; e.g. Cowie, Gupta, & Dawers, 2000; Gawthorpe & Leeder, 2000; Ziegler & Cloething, 2004). The resulting strong topographic gradients evolve with time and determine source and sink areas in the rift, with the possibility of multiple sources of sediment, including the rift shoulder and intra-rift fault blocks operating at the same time. Axial and transverse drainage in deep-water extensional basins

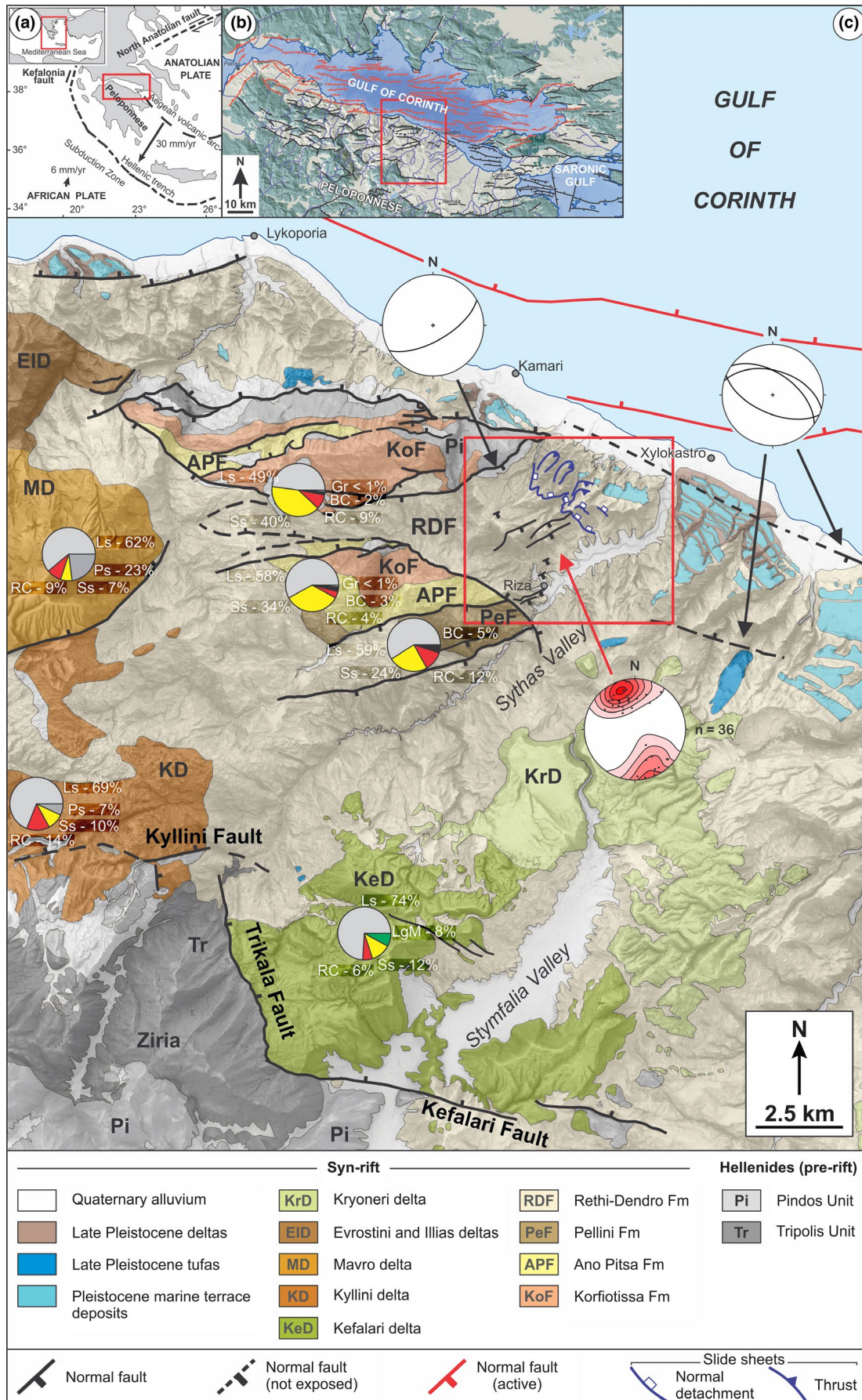
Highlights

- Field-based study of lacustrine deep water Plio-Pleistocene deposits from the Corinth Rift
- Identification of axial and transverse subaqueous drainage sedimentary systems
- Multiple sediment sources (hinterland vs. intrabasin) differentiated by clast composition analysis
- Hangingwall tilting phases controlled sediment pathways and overall stratigraphic stacking patterns

are widely recognized features (e.g. McArthur et al., 2016; Papatheodorou & Ferentinos, 1993; Smith & Busby, 1993; Zhang & Scholz, 2015; Zhang et al., 2014), often included in rift basin sedimentary models (e.g. Gawthorpe & Leeder, 2000; Leeder & Gawthorpe, 1987; Ravnås & Steel, 1998). Nevertheless, studies on deep-water syn-rift deposits tend to concentrate on the processes occurring on the subaqueous slope systems associated with marginal basin fault scarps (e.g. Ferentinos et al., 1988; Henstra et al., 2016; Leeder et al., 2002; Leppard & Gawthorpe, 2006; Strachan et al., 2013) and more rarely, on the deposits sourced from hangingwall dipslopes (e.g. Jackson et al., 2011; Ravnås & Steel, 1997). This study addresses the need for linkage of the various parts of deep-water sedimentary systems in rift basins and analyses their evolution in conjunction with normal fault growth, the role of intrabasinal highs as sediment sources and structural control of basin floor gradients. Addressing such issues has important impact on rift basin studies in general, for the understanding of deep-water drainage behaviour and also their application to subsurface exploration and production.

This study focuses on the evolution of a deep-water sedimentary system and its interaction with the extensional structures in a rift axis depocentre located approximately

FIGURE 1 Location maps. (a) Aegean/Mediterranean tectonic setting; red rectangle indicates the location of (b). (b) Corinth Rift regional map; red rectangle indicates the location of (c). (c) Geological map of the central Corinth Rift, modified from Gawthorpe, Leeder, et al. (2017). Active faults are indicated in red and fossilized ones in black. The orientations of the depocentre main boundary fault systems are indicated with stereonet diagrams while the orientations of the faults internal to the depocentre are shown with a fault-plane pole distribution diagram. Pie diagrams show the results of clast composition analysis on different sources of sediment to the RDF such as deltas (Kyllini, Kefalari and Mavro) and intrabasinal highs with exposures of previous syn-rift units (Korfiotissa Formation, Ano Pitsa Formation and Pellini Formation). Ls: limestones, Ss: sedimentary rocks (mainly sandstones), Ps: phyllites, RC: red chert, BC: black chert, Gr: granitoids. The complete dataset used for the clast composition analysis is presented in the Supplementary data section



12 km basinwards of the contemporaneous margin coastline and at the exit of a structurally controlled sediment fairway, ~15 km along-strike of its deltaic sediment source. The studied deposits are the Plio-Pleistocene Rethi-Dendro Formation (hereafter RDF) exposed in the Amphithea fault block, Corinth Rift, Greece (Figure 1). The study of deep-water deposits in extensional settings is often a challenge because the deposits tend to be buried in the subsurface. In contrast, the Corinth Rift represents one of a very few basins in the world where early syn-rift deposits are presently exposed due to uplift of the rift shoulder without any inversion of the extensional structures. This represents nearly unique conditions for the study of the original geometry of deep-water deposits and their link to the structural evolution of a rift depocentre. Moreover, the Corinth Rift is an active extensional basin still in the relatively early stages of rift evolution. Consequently, this study offers important insights into the development of early rift deep-water deposits that are usually eroded from the rift shoulders in more mature basins such as the Red Sea, North Sea and the Atlantic rifted margin in general (e.g. Steckler, Berthelot, Lyberis, & Pichon, 1988; Nøttvedt et al., 2000; Ravnås et al., 2000; Bosworth, Huchon, & McClay, 2005; Torsvik, Rouse, Labails, & Smethurst, 2009; Moulin, Aslanian, & Unternehr, 2010).

2 | GEOLOGICAL SETTING

The Corinth Rift originated ~5 Ma from N-S extension occurring between the North Anatolian fault and the Kefalonia fault/Hellenic subduction zone (Collier & Dart, 1991; Leeder et al., 2008) and cuts across the N-S striking Hellenide thrust belt (Figure 1). The rift structure is characterized by mainly E-W striking normal fault segments up to 20 km in length, that mainly dip towards the north and can achieve several kilometres of displacement. Fault activity in the rift progressively migrated from S to N with present-day extension concentrated on the fault network developed along the southern coast of the Gulf of Corinth. Activity of the rift is characterized by two main phases (Gawthorpe, Leeder, et al., 2017): Rift 1 from 5.0–3.6 to 2.2–1.8 Ma and Rift 2 from 2.2–1.8 Ma to present. Rift 1 is exposed mainly on the southern margins of the Corinth Gulf and represents the evolution from fluvial and palustrine conditions during rift initiation to the establishment of a deep-water lake as the creation of accommodation progressed. At the onset of Rift 2, fault activity shifted towards the north, causing the subsequent uplift and erosion of the fault blocks that were active during Rift 1. The oldest extensional structures are found fossilized along the northern Peloponnese up to 30–40 km south of the modern southern shoreline of the Gulf of Corinth.

The pre-rift stratigraphy in the central Corinth rift area (Figure 1) corresponds to the nappe units of the Hellenide

thrust belt. From structurally deeper to shallower levels, these are: (1) the Phyllites-Quartzites Unit, with high-pressure mica schists, phyllites, quartzites and rare metabasalts; (2) the Tripolis Unit, which comprises a dolomitized Upper Triassic to Upper Eocene shelf carbonate sequence and an Upper Palaeozoic to Lower Triassic volcano-sedimentary complex at the base (Tyros beds), capped by Lower Eocene to Oligocene flysch; and (3) the Pindos Unit, mainly formed of Mesozoic pelagic limestones and chert with volcanic and clastic rocks at the base and Palaeocene to Eocene flysch sequences towards the top (e.g. Pe-Piper & Piper, 1991; Skourtsos, Kranis, Zambetakis-Lekkas, Gawthorpe, & Leeder, 2016).

Rifting is interpreted to have started in the latest Miocene or early Pliocene based on radiometric dating (Collier & Dart, 1991; Leeder et al., 2008) and the syn-rift succession in the central Corinth rift has been subdivided by Gawthorpe, Leeder, et al. (2017) into the following stratigraphic units, from base to top: the fluvial Korfiotissa Formation, the floodplain to palustrine Ano Pitsa Formation, the lower slope to pro-delta Pellini Formation, the lacustrine RDF and the laterally equivalent Kefalari, Kyllini, Mavro, Evrostini and Illias deltas, unconformably overlain by the Kryoneri delta, Pleistocene marine terraces, tufas and deltas and present-day sedimentary systems (Figure 1). The RDF in the Amphithea fault block is the focus of this study. However, the RDF and similar rock units have been mapped together through several fault blocks (Bornovas, Lalechos, Filippakis, Christodoulou, & Tsaila-Monopoli, 1972; Koutsouveli, Mettos, Tsapralis, Tsaila-Monopoli, & Ioakim, 1989; Tataris, Maragoudakis, Kounis, Christodoulou, & Tsaila-Monopoli, 1970; Tsoflias, Fleury, & Ioakim, 1993) that were active at different times during both Rift 1 and Rift 2 with ages between late Pliocene to middle Pleistocene (see Gawthorpe, Leeder, et al., 2017).

3 | THE AMPHITHEA FAULT BLOCK

The present-day structural configuration of the Amphithea fault block is mainly defined by the presence of two intra-basinal highs (the Amphithea and Xylokastro horsts) and a south-dipping fault lying in the subsurface close to the coast towards the north. This fault is interpreted to be the continuation of the Melissi fault exposed to the southeast of the city of Xylokastro (Gawthorpe, Leeder, et al., 2017) (Figures 1 and 2). The hangingwall consistently dips towards the northeast where more than 1,300 m of the RDF are exposed in continuous cliff sections on the western margin of the Sythas Valley. The base of the RDF is not exposed in this fault block and its top is eroded by an angular unconformity developed at the base of a complex of down-stepping Pleistocene delta lobes and marine terrace deposits (Gawthorpe, Leeder, et al., 2017). The normal

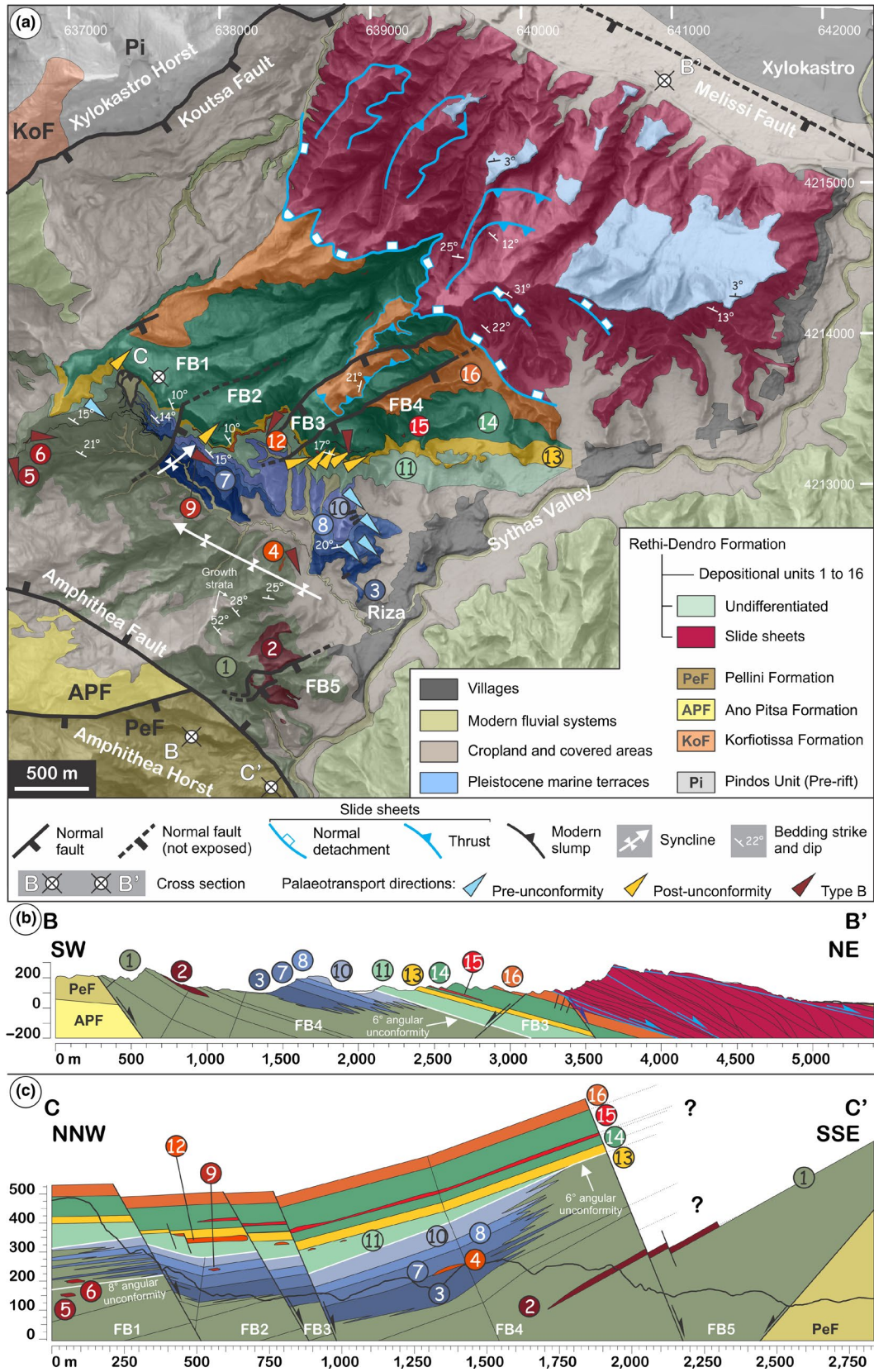


FIGURE 2 Study area in the Amphithea fault block. (a) Geological map. (b) Cross section B-B'. (c) Cross section C-C' with reconstructed stratigraphy above present day topography. The different stratigraphic units within the RDF are marked with numbered coloured circles (Figure 3). The internal normal faults in the depocentre define fault blocks (FB) 1, 2, 3, 4 and 5. Note the occurrence of extensive slide sheets towards the northern sector of the Amphithea fault block

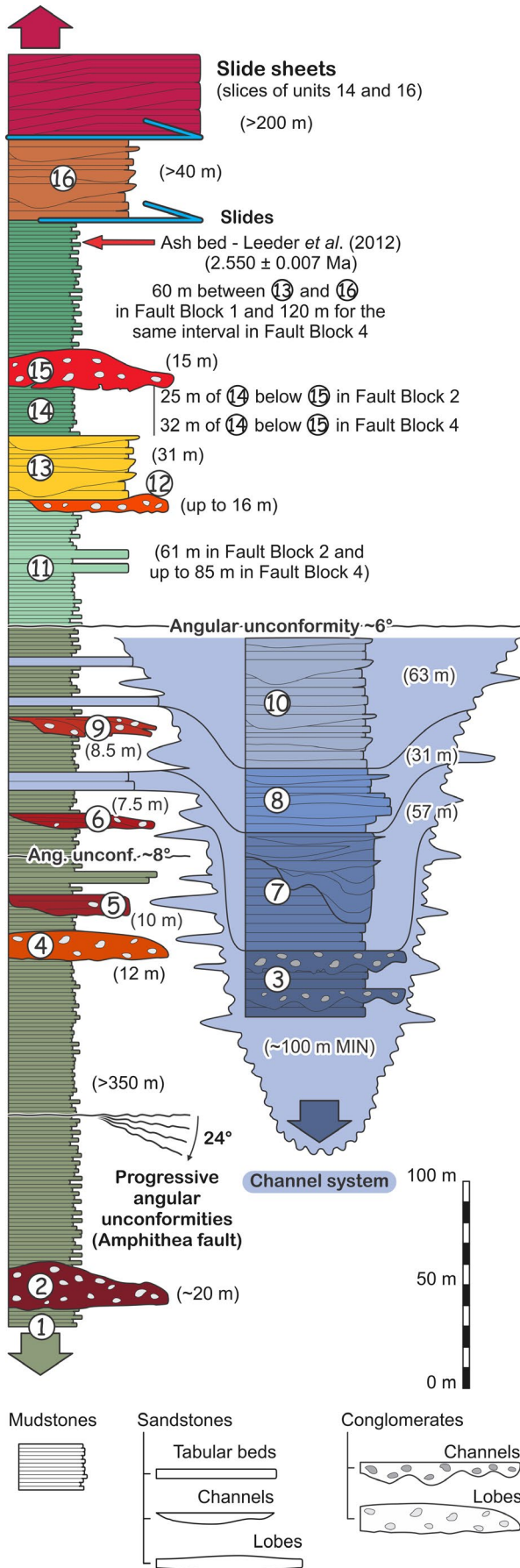


FIGURE 3 Stratigraphic column of the RDF in the Amphithea fault block (Figure 2). The different units are numbered from 1 to 16 following their stratigraphic order. Note that the channel system represented by units 3, 7, 8 and 10 is laterally equivalent to units 1, 4, 5, 6 and 9. The entire interval depicted in this column corresponds to 615 m. Red arrow indicates the approximate position of the ash bed studied by Leeder *et al.* (2012)

faults in the hangingwall have a NE-SW orientation, parallel to the Koutsas fault at the southeastern border of the Xylokastro Horst and highly oblique to perpendicular to the northern and southern boundary fault systems of the Amphithea fault block (Figures 1 and 2). The smaller-scale fault blocks within the Amphithea area are designated as Fault Blocks 1, 2, 3, 4 and 5 (Figure 2).

The horst configuration of the Amphithea and Xylokastro intra-basinal highs is a recent feature that was not fully developed during deposition of the RDF in the Amphithea fault block (Gawthorpe, Leeder, *et al.*, 2017). The Koutsas and Melissi fault planes were exposed during the deposition of RDF in the study area, but the Amphithea fault is interpreted to have been buried and, by propagating-upwards, has created a syn-sedimentary forced-fold (Gawthorpe, Leeder, *et al.*, 2017). The normal faults in the hangingwall have a throw that varies from approximately 20–70 m. Differences in thickness across these faults indicate that they were active during the deposition of the RDF (Figures 2 and 3).

4 | METHODOLOGY

Field-based study involved analysis of exposures 100–250 m high in near-vertical cliffs of the western margin of the Sythas Valley (Figures 2 and 3). This was achieved by detailed field mapping and sedimentary logging, combined with 3D digital outcrop analysis acquired from terrestrial LiDAR, photogrammetry and UAV mapping techniques. This approach allowed the integration of small and large-scale observations into one common group of digital outcrop models that was subsequently interpreted with the aid of Virtual Reality Geological Studio software (VRGS, *e.g.* Hodgetts, 2009; Rarity *et al.*, 2014). By these means, measurements from bed to fault block scale of bedding and rock body orientation and the dimensions and orientation of unit boundaries were obtained. The analysis of bedding measurements at fault block scale allowed for the detection of angular unconformities within the stratigraphy of the RDF (Figure 4) and the effect of basin-floor tilting in the evolution of the subaqueous environment (*e.g.* Ravnås & Steel, 1997; Muravchik *et al.*, 2018).

In order to identify sediment sources for the different deposits in the RDF, clast composition counts were performed on conglomerate-grade beds within this formation and its surrounding stratigraphic units. The method involves registering the composition of the clasts along a regular matrix in

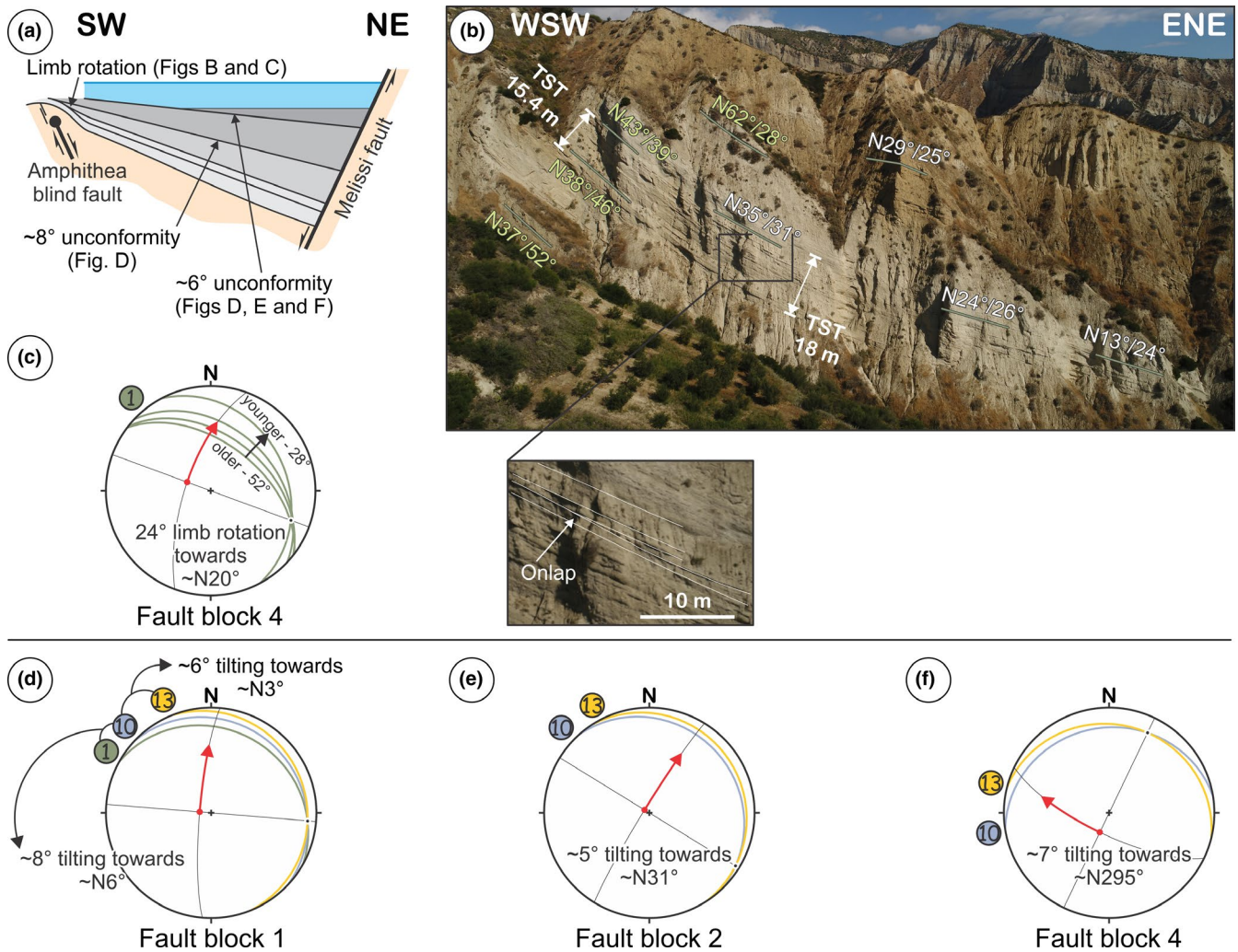


FIGURE 4 Basin-floor tilting events within the Amphithea depocentre (Figure 2). (a) Schematic representation of the Amphithea fault block showing the relative position of the growth strata and angular unconformities measured in b, c, d, e and f. Diagram not to scale. (b) and (c) Limb rotation and growth-strata associated to the growth of the Amphithea fault found in Fault Block 4 (Figure 2a). (b) Field photograph with indications of bedding dip and strike measured from a digital outcrop model. The bedding values indicated in green are represented in the stereonet diagram in (c). Note the increase in thickness down-dip the monocline limb, from 15.4 to 18 m in the indicated interval (TST: true stratigraphic thickness). The expanded view shows stratal onlap up-dip onto the limb of the monocline. Field of view is approximately 250 m wide. (c) Stereonet diagram showing the direction of limb rotation. The bedding dip values decrease from 52° to 28° upwards in the stratigraphy of the growth-strata. This decrease in dip reflects the progressive rotation of the limb of the monocline developed on top of the blind Amphithea fault during its growth (Figure 4a). The stereonet diagrams in d, e and f display plane values that represent the best fit plane for surfaces tracked along the extent of each fault block in the digital outcrop models: Unit 1 internal boundary (d) and the top boundaries of units 10 and 13 (d, e and f). The angular unconformity observed within Unit 1 is represented by the difference in dip between the measurements of units 1 and 10 (d) (Figures 2 and 3). The angular unconformity observed at the base of Unit 11 is represented by the difference in dip between the measurements of units 10 and 13 (d, e and f) (Figures 2 and 3). The unconformity at the base of Unit 11 cannot be measured properly in Fault Block 3 due to the quality of the exposures at that interval. The difference in the direction of tilt among fault blocks 1, 2 and 4 (d, e and f) shows the local effect of the internal growing normal faults over the larger scale tilting experienced by the Amphithea hangingwall as a whole towards the NNE. Note that the red arrow in the stereonet diagrams only indicates the direction of tilting, but is not scaled to match its magnitude

which node spacing is defined by the mean clast size of the bed under scrutiny (Muravchik, Bilmes, D'Elia, & Franzese, 2014). Percentage pie charts (Figure 1) and spider diagrams (Figure 5) are used to illustrate the analysis and the complete dataset is presented as Supplementary data.

Analysis of the orientation of the sedimentary systems in the RDF is mainly based on measurements of rock body orientation such as lobe axes and channel thalwegs (e.g. Fabuel-Pérez, Hodgetts, & Redfern, 2009; Muravchik et al., 2014; Rarity et al., 2014) from the digital outcrop models (Figure

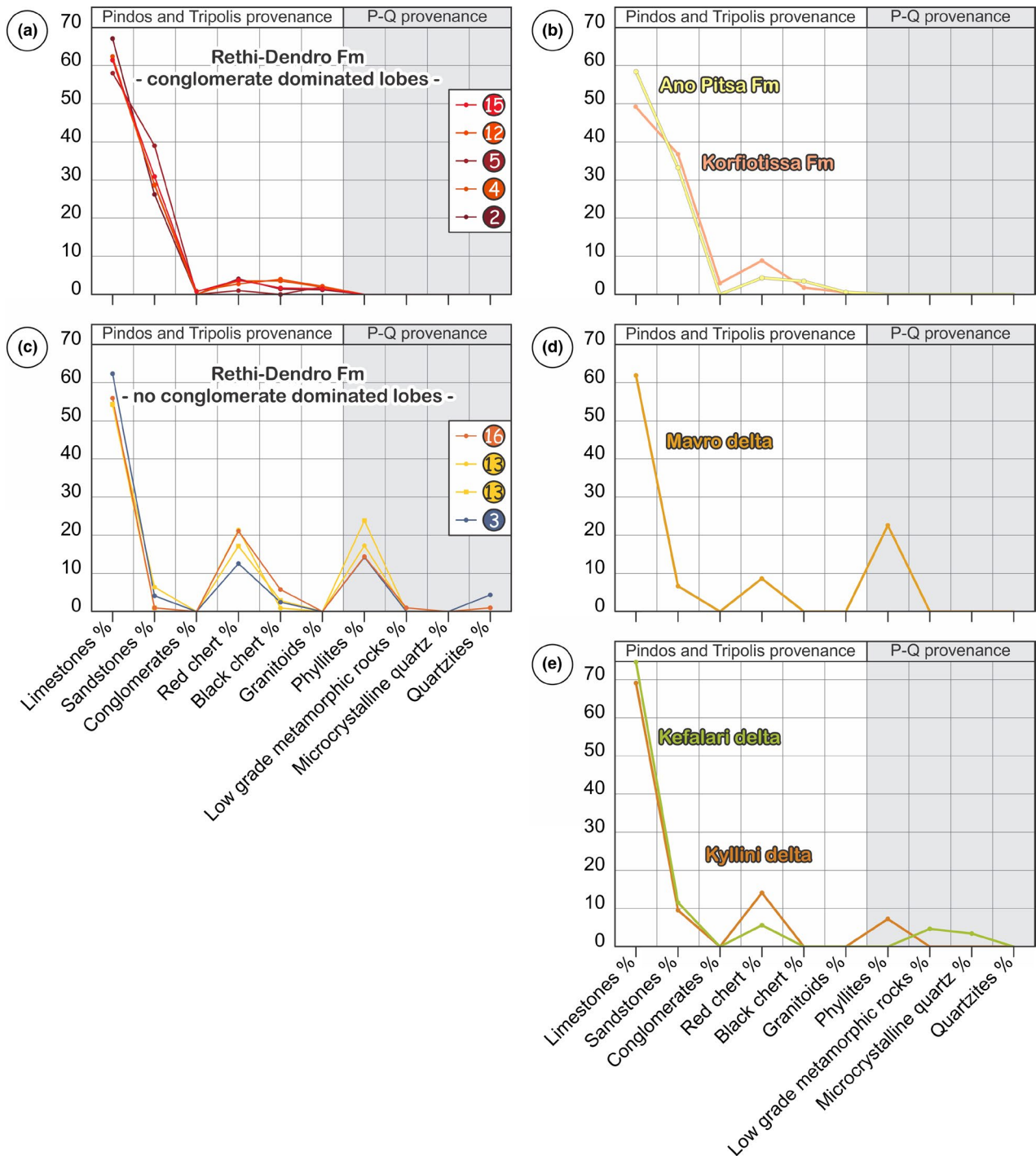


FIGURE 5 Clast composition analysis. Diagrams show the proportion of the different clast lithologies expressed as percentages for depositional units within the RDF (a and c) and their possible sources (b, d and e). The lithologies of the clasts are grouped according to their provenance (i.e. Pindos and Tripolis units vs. Phyllites-Quartzites Unit). (a) Values measured in the conglomerate-dominated lobes, units 2, 4, 5, 12 and 15, have a great affinity to those registered for the Korfiotissa and Ano Pitsa formations (b). (c) In contrast, the values measured in the other type of units (e.g. units 3, 13 and 16) have a provenance akin to the one measured for the Mavro delta (d) and different from other sources of the RDF such as the Kyllini or Kefalari deltas (e). The complete dataset used for the clast composition analysis is presented in the Supplementary data section

6). Measurements were complemented by palaeocurrent directions obtained from logged sections (e.g. current ripples and trough-cross stratification). In order to better evaluate

the significance of each directional feature, all measurements were weighted according to their size (cross sectional area in m²; Figure 6d).

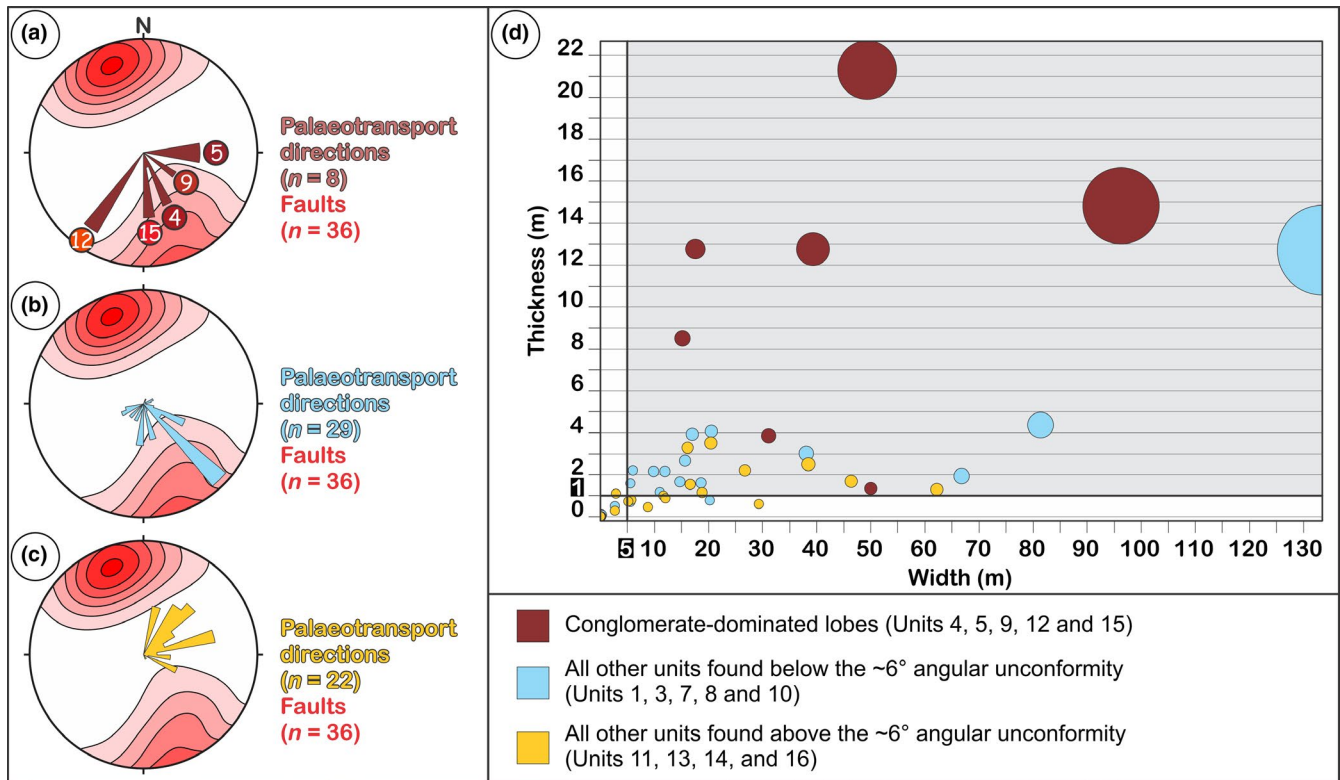


FIGURE 6 Palaeotransport analysis of the RDF in the Amphithea fault block. (a, b and c) Rose diagrams of palaeotransport directions superposed to the fault plane pole distribution diagram for the faults internal to the Amphithea fault block (Figure 1). (a) Palaeotransport directions measured in the conglomerate-dominated lobes (units 4, 5, 9, 12 and 15; indicated with numbered coloured circles on the rose diagram) (Figures 2 and 3). (b) Palaeotransport directions measured in all other units found below the ~6° angular unconformity (units 1, 3, 7, 8 and 10) (Figures 2 and 3). (c) Palaeotransport directions measured in all other units found above the ~6° angular unconformity (units 11, 13, 14 and 16) (Figures 2 and 3). (d) Palaeotransport data plotted according to the size of the measured directional features (lobe axes, channel thalwegs, scours, current ripples and trough-cross stratification). The size of the circles is scaled to represent the cross sectional area (m²) of the directional features measured in this study. Note that the majority of the measured features are thicker than 1 m and larger than 5 m in length

5 | THE RETHI-DENDRO FORMATION IN THE AMPHITHEA FAULT BLOCK

Deposition of the RDF in the Amphithea fault block occurred during Rift 1 in a deep-water lacustrine environment (Gawthorpe, Leeder, et al., 2017). There is no evidence for a connection with a marine basin and no sequence stratigraphic framework exists. Sixteen stratigraphic units are recognized in this study for the lower half of the formation based on rock body geometry, dimensions, internal architecture, grain size distribution and boundaries (Figures 2 and 3). The upper half of the formation consists of a series of slide sheets of NE vergence, composed of slices of units 14 and 16 (Figures 2a, b and 3). Although the exact age of the formation is not known, the 2.55 Ma age of an ash bed close to the base of Unit 16 (Leeder et al., 2012) means that the Pliocene-Pleistocene boundary probably lies within Unit 14 (Figure 3).

Tilting of the hangingwall in the Amphithea fault block occurred mainly towards the NNE, as it is revealed by the consistent dip direction of the RDF strata in that same

direction (Figure 2). Analysis of the angular unconformities within the RDF and differences in bedding dip values reveal the existence of discrete basin-floor tilting events of varying magnitude (Figure 4) that are documented from the following three cases: 1) rotation of a monocline limb associated to the Amphithea fault (Figure 4b, c); 2) an angular unconformity of ~8° (Figures 3 and 4d) an angular unconformity of ~6° (Figure 4d, e, f). Evidence for the rotation of the monocline limb associated to the Amphithea fault lie in a series of spatially restricted progressive angular unconformities that result from fanning geometries recorded within Unit 1 strata. These are found within the first 500 m of the hangingwall of the Amphithea fault in Fault Block 4 (between points 1 and 4 in Figures 2a and 3). The exposures display thickening of stratal packages down-dip the monocline limb (Figure 4b) and conversely, subtle onlap stratal terminations up-dip onto the monocline limb (expanded view in Figure 4b). Growth strata dip towards the NNE with the magnitude of dip decreasing consistently upwards and away from the Amphithea fault (Figure 4b, c). This configuration is interpreted to indicate that the fault was a blind growth fault with a monocline

flexure developed on top (Gawthorpe, Leeder, et al., 2017). The $\sim 8^\circ$ unconformity occurs within Unit 1, between the positions marked by the lobes of units 5 and 6 (Figures 2c, 3 and 4d). As this unconformity is only exposed in Fault Block 1 (Figure 4d), it is not possible to assess its actual spatial extent. However, its NNE dip direction, almost coincident with the $\sim 6^\circ$ unconformity in Fault Block 1 (Figure 4d), suggests its origin related to the tilting of the Amphithea hangingwall towards the northern boundary fault system. The $\sim 6^\circ$ unconformity is found at the base of Unit 11 and can be traced from Fault Block 1 to 4 (Figures 2b, c, 3 and 4d, e, f). The occurrence of the $\sim 6^\circ$ unconformity at exactly the same stratigraphic position in fault blocks 1, 2, 3 and 4 indicates that the process behind its origin was of a larger scale than these normal faults and is interpreted to have been linked to the tilting of the Amphithea fault block as a whole (Figures 2 and 4a, d, e, f). Variations in the orientation of the $\sim 6^\circ$ unconformity measured between fault blocks 1, 2 and 4 (Figure 4d, e, f), result from the competing effect of backtilting faults of different orientations (i.e. Melissi fault vs. internal normal faults), showing that the internal normal faults were active during its development, as it is suggested by the differences in thickness of the unit immediately above the unconformity (Unit 11) between Fault Blocks 1, 2, 3 and 4 (Figures 2 and 3). The fact that the different depositional units in the formation consistently dip towards the NNE, together with the decrease in the magnitude of the dip of the bedding and angular unconformities upwards in the stratigraphy of the RDF (Figures 2 and 4) implies that tilting towards the northern boundary fault system at hangingwall scale was a first-order control in the evolution of the depocentre (e.g. Ravnås & Steel, 1997; Muravchik et al., 2018) and that the internal normal faults played a more local role (Figures 2a, c and 4).

The stratigraphic interval below the $\sim 6^\circ$ unconformity is characterized by more than 350 m of mudstone-dominated deposits represented by Unit 1, punctuated by the conglomerate-dominated lobes of units 2, 4, 5, 6 and 9 (Figures 2 and 3). Laterally equivalent to these units there is a channel system composed of units 3, 7, 8 and 10, which reaches 250 m at its thickest, close to the locality of Riza (Figures 2 and 3), where it was mapped as the Riza Member by Gawthorpe, Leeder, et al. (2017). Units 8 and 10 in the channel system thin and interdigitate with Unit 1 towards the west (Figures 2 and 3), above the $\sim 8^\circ$ unconformity. The lateral relationship between Unit 1 and the channel system below the $\sim 8^\circ$ unconformity is less clear due to the nature of the exposures. Above the $\sim 6^\circ$ unconformity, the formation is characterized by the alternation of mudstone-dominated units (11 and 14) with intercalated conglomerate-dominated lobes (units 12 and 15) on the one hand and sandstone-dominated units (13 and 16) on the other (Figures 2 and 3).

5.1 | Clast composition

The RDF and its laterally equivalent deposits are the oldest to contain metamorphic clasts derived from the lowest exposed structural levels of the Hellenide thrust belt, the Phyllites-Quartzites Unit, reflecting the progressive uplift and erosion of the rift shoulder (e.g. Gawthorpe, Leeder, et al., 2017; Rohais, Eschard, Ford, Guillocheau, & Moretti, 2007). Gawthorpe, Leeder, et al. (2017) suggested the Mavro delta as the source of the RDF in the Amphithea fault block based on the relative abundance of phyllite clasts in both units and their location and stratigraphic position. Closer inspection, however, reveals two clear compositional patterns. The main bulk of the deposits have a signature compatible with a mixed provenance from the Phyllites-Quartzites Unit, the Pindos Unit and the Tripolis Unit in the pre-rift. However, the conglomerate-dominated lobes of units 2, 4, 5, 6, 9, 12 and 15 (Figure 3) contain granitoid clasts that are completely absent from the other RDF depositional units.

In order to better constrain the provenance of the deposits and assess the contribution of potentially multiple sediment sources, clast composition analyses were performed on selected RDF depositional units, on the closest delta units to the Amphithea fault block (i.e. Kyllini, Kefalari and Mavro, Figure 1) and on early rift deposits exposed on the Amphithea and Xylokastro horsts (Figure 1). The different compositions detected fall in the following categories: (1) limestone, sandstone and conglomerate clasts sourced from the Pindos and Tripolis units; (2) red chert, black chert and granitoid clasts sourced from the Pindos Unit and (3) phyllite, low-grade metamorphic rock, microcrystalline quartz and quartzite clasts sourced from the Phyllites-Quartzites Unit (Figure 5 and Supplementary data). It is important to note that the granitoid lithologies in the Pindos Unit are clasts in conglomerates found in the flysch and no other granitoid sources are known for the entire Peloponnese (e.g. Pe-Piper & Koukouvelas, 1990, 1992; Pe-Piper & Piper, 1991). The granitoid-bearing provenance of the conglomerate-dominated lobes is similar to the syn-rift Korfiotissa and Ano Pitsa formations (Figure 5a and b), whereas the provenance of the rest of the RDF depositional units matches the Mavro delta (Figure 5c and d). This near coincidence in the clast composition between the Mavro delta (Figure 5d) and the deposits with a Phyllites-Quartzites provenance in the RDF (Figure 5c) and the fact that the deposits in Kefalari and Kyllini deltas are clearly different, contrasts with the compositional patterns observed for the deposits in the Kyllini and Kefalari deltas (compare Figure 5c, d on the one hand and 5e on the other). Although the Kyllini and Kefalari delta deposits also contain lithologies derived from the Phyllites-Quartzites Unit, their composition is different enough to exclude them as important sources of the RDF

in the Amphithea depocentre. The proportion of phyllites in the Kyllini deposits (Figure 5e) is considerably smaller than in the case of the deposits with a Phyllites-Quartzites provenance in the RDF (Figure 5c). Any contribution of clasts from the Kyllini deposits should significantly decrease the content in phyllite clasts in the RDF in a proportion that is not observed in the compositional data (Figure 5). The proportion of limestones in both the Kyllini and Kefalari deposits (Figure 5e) is higher than in the case of the deposits with a Phyllites-Quartzites provenance in the RDF (Figure 5c). As limestones are one of the most resistant lithologies found in the clasts, contribution from these two deltas should increase the content of limestones in the RDF and that pattern is not observed (Figure 5c). From the clast composition analysis illustrated in Figure 5, it is evident that the main sediment source for the Amphithea depocentre originated in the rift shoulder to the south via the Mavro delta, ~15 km W of the study area, with minor sediment sources from local intrabasinal highs or from the northern margin of the rift.

5.2 | Palaeotransport directions

The directional structures measured in the RDF (lobe axes, channel thalwegs, scours, current ripples and trough-cross stratification) can be divided into the following three clusters: (1) the conglomerate-dominated lobes, (2) all other units below the ~6° unconformity and (3) all other units above the ~6° unconformity (Figure 6). The analysis shows a clear rearrangement of the transport direction from mainly transverse to the strike of the internal faults in the units below the ~6° unconformity (Figure 6b) to subparallel to fault strike in the units above the unconformity (Figure 6c). This pattern cannot, however, be discerned for the conglomerate-dominated lobes (Figure 6a). The orientation of these lobe axes suggests in any case that their sources were located towards the northwest of the study area. This observation is compatible with the present-day distribution of older units of similar composition (i.e. units containing granitoid clasts and lacking phyllites and other metamorphic clasts; Figure 5a and b), and it is therefore suggested that the conglomerate-dominated lobes were sourced from local intrabasinal highs towards the Xylokaastro horst area (Figure 1), detached in origin from the sedimentary system fed by the Mavro delta (Figure 5).

6 | DEPOSITIONAL ELEMENTS

Based on rock body geometry, dimensions, internal architecture, grain size distribution and unit boundaries, the 16 stratigraphic units identified in this study (Figure 3) can be grouped into six different types of depositional elements

(Figure 7): type A—mudstone-dominated sheets (1, 11 and 14); type B—conglomerate-dominated lobes (2, 4, 5, 6, 9, 12 and 15); type C—conglomerate channel belts and sandstone sheets (3); type D—sandstone channel belts (7); type E—sandstone-dominated broad shallow lobes (8) and type F—sandstone-dominated sheets with broad shallow channels (10, 13 and 16). Their description and analysis is based on the approach made by Talling, Masson, Sumner, and Malgesini (2012) for subaqueous sediment density flows and is presented in the following sections.

6.1 | Type A - mudstone-dominated sheets (Units 1, 11 and 14)

Mudstone-dominated units 1, 11 and 14 are composed of stacked individual mudstone-dominated sheets that range between 8 and 25 m in thickness and can be traced for more than 2.5 km (Figures 7a, 8a, b and 9). The proportion of sandstone beds in these sheets is generally between 18% to 27% of the thickness. The deposits are characterized by 1 to 7 cm thick mudstone beds intercalated with 1 to 2 cm thick siltstones and 3 to 24 cm thick very fine to lower medium sandstones (Figures 8a and 9b). Mudstones in the RDF are predominantly composed of variable proportions of calcium carbonate and argillaceous clay, however, due to uncertainty in determining this proportion in the field, the grain-size equivalent term mudstone is used in this study. The mudstones are found as tabular laminated beds and the sandstones constitute massive or laminated tabular beds with normal grading, typically with asymmetrical rippled tops. Plant remains are frequently found as small broken fragments (1 to 7 mm) within the fine lamination or as well preserved stems and leaves at the base of the beds (Figure 9c). Moderate to high bioturbation is common, mainly represented by non-ornamented single vertical tubes 1 to 2 cm long (Figure 9d). Rare 4 to 14 m thick intervals enriched in sandstone beds (up to 36 to 44% sandstones) of sheet or lenticular geometry intercalate the mudstone sheets (Figure 8b). These sandstone beds are up to 45 cm thick and the grain size reaches lower coarse sand grade. They are frequently normal-graded and can be either structureless or develop current ripples at the top. The thickest sandstone beds preserve accumulations of muddy intraclasts at the base or as thin lenses. Very rarely, conglomerate lenses containing pebbles and cobbles up to 8 cm and 10 to 30 cm intraclasts supported in a sandy matrix are found, reaching 50 cm in thickness (Figure 9e). The sandstone enriched intervals found in Unit 1 can be traced laterally for several hundreds of metres towards the east until they link with units 3, 7, 8 or 10 in the channel system (Figure 3). To the west, the proportion of sandstone beds decreases progressively and the intervals terminate in tapering wedge geometries that pinch out over ~100 m (Figure 9f).

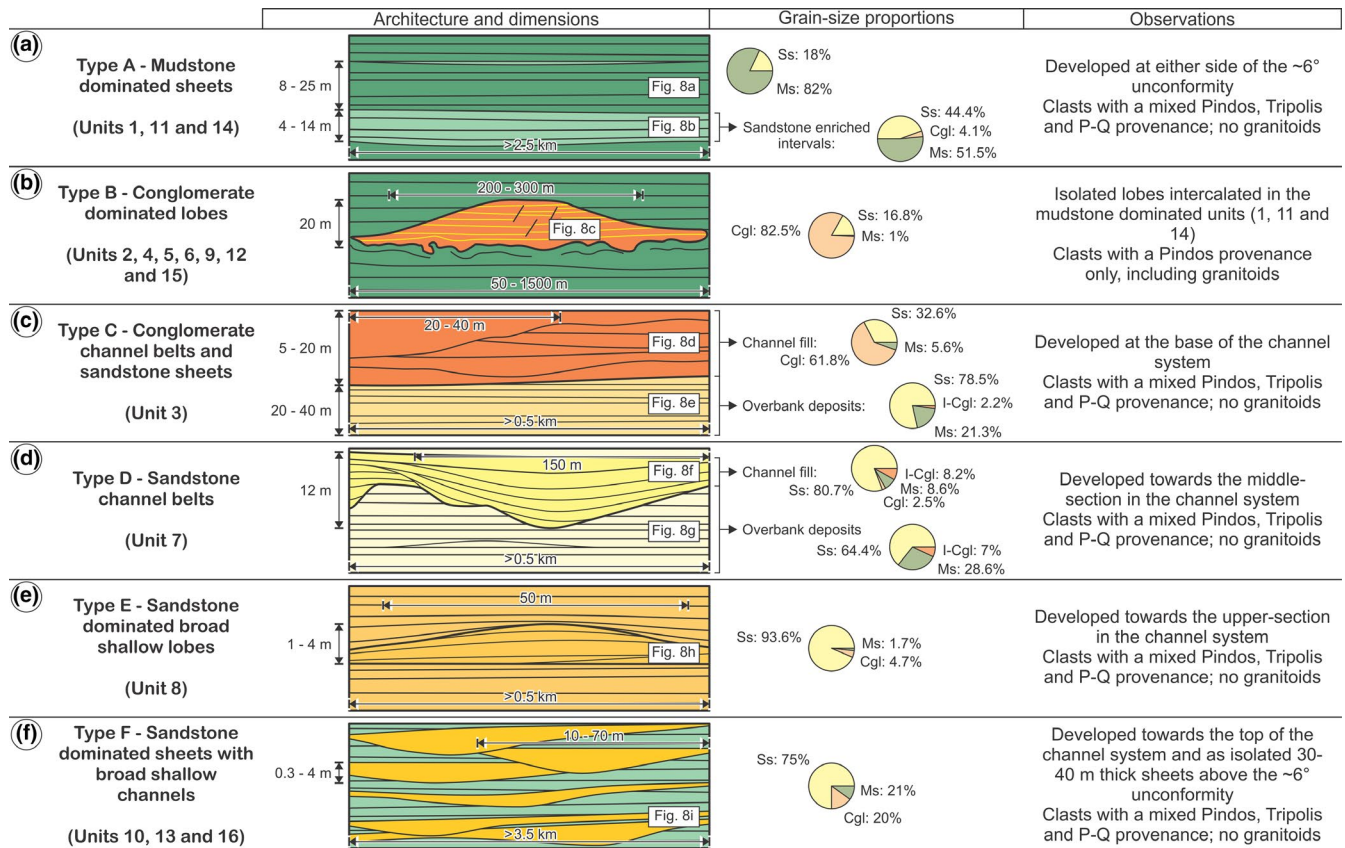


FIGURE 7 Main characteristics of the different types of depositional elements recognized in the RDF exposed in the Amphithea fault block. Box sketches represent the architectural style of each element. The corresponding sedimentary logs (Figure 8) are indicated on each sketch. Grain-size proportions in the rock bodies are shown as percentage values represented by pie diagrams. Cgl: conglomerates, I-Cgl: intraclast conglomerates, Ss: sandstones, Ms: mudstones. P-Q: Phyllites-Quartzites Unit

The predominance of mudstone in type A units together with their planar geometry at the km scale indicates a subaqueous low energy environment below storm-wave base and with very low gradients, such as a basin floor plain (e.g. Johnson et al., 2001; Sumner et al., 2012). The mudstone beds are interpreted to represent suspension fallout and deposition from turbulent mud clouds (cf. Talling et al., 2012), whereas the occurrence of relatively thin sandstone beds with traction structures such as lamination and ripples indicate deposition from turbiditic flows (e.g. Dasgupta, 2003; Talling et al., 2012). The planar remains reflect the overall subaerial source of the depositional system. The development of coarser and thicker-bedded sandstone-enriched intervals with accumulation of intraclasts is interpreted as the progradation of distal lobes over the basin floor plain (e.g. Hodgson et al., 2006; Prélat & Hodgson, 2013; Prélat, Hodgson, & Flint, 2009; Sychala, Hodgson, Stevenson, & Flint, 2017). The fact that the sandstone-enriched intervals in Unit 1 physically link with units 3, 7, 8 or 10 in the channel system, together with their progressive reduction in sandstone content away from the channel system and the characteristic tapering geometry of their terminations (Figure 9f), suggest that they represent in this particular case, the lateral fringes of the channel system

over the basin floor plain, sharing the same characteristics described for channel levees in other settings (e.g. Di Celma, Brunt, Hodgson, Flint, & Kavanagh, 2011; Morris, Hodgson, Brunt, & Flint, 2014; Posamentier & Kolla, 2003).

6.2 | Type B - conglomerate-dominated lobes (Units 2, 4, 5, 6, 9, 12 and 15)

The conglomerate-dominated lobes have convex tops with a typical wavelength of 100 to 300 m (Figures 7b and 10a) and occur as isolated bodies intercalated in the mudstone-dominated units 1, 11 and 14 (Figures 2 and 3). The lobes range in thickness from 5 to 20 m and their lateral extent is 50 to 1,500 m. They are conspicuously affected by syn-sedimentary internal deformational features such as normal faults and clastic intrusions that result in the development of highly irregular bases (Figures 7b, and 10b, d). Internally, lobes are composed of stacked tabular conglomerate beds 0.1 to 1.6 m thick, intercalated with 4 to 70 cm thick sandstone lenses (Figures 7b, 8c and 10c). The proportion of conglomerates in these deposits varies from 60% to 82%. Conglomerate clasts vary in size from 1 to 15 cm and are supported by a poorly to

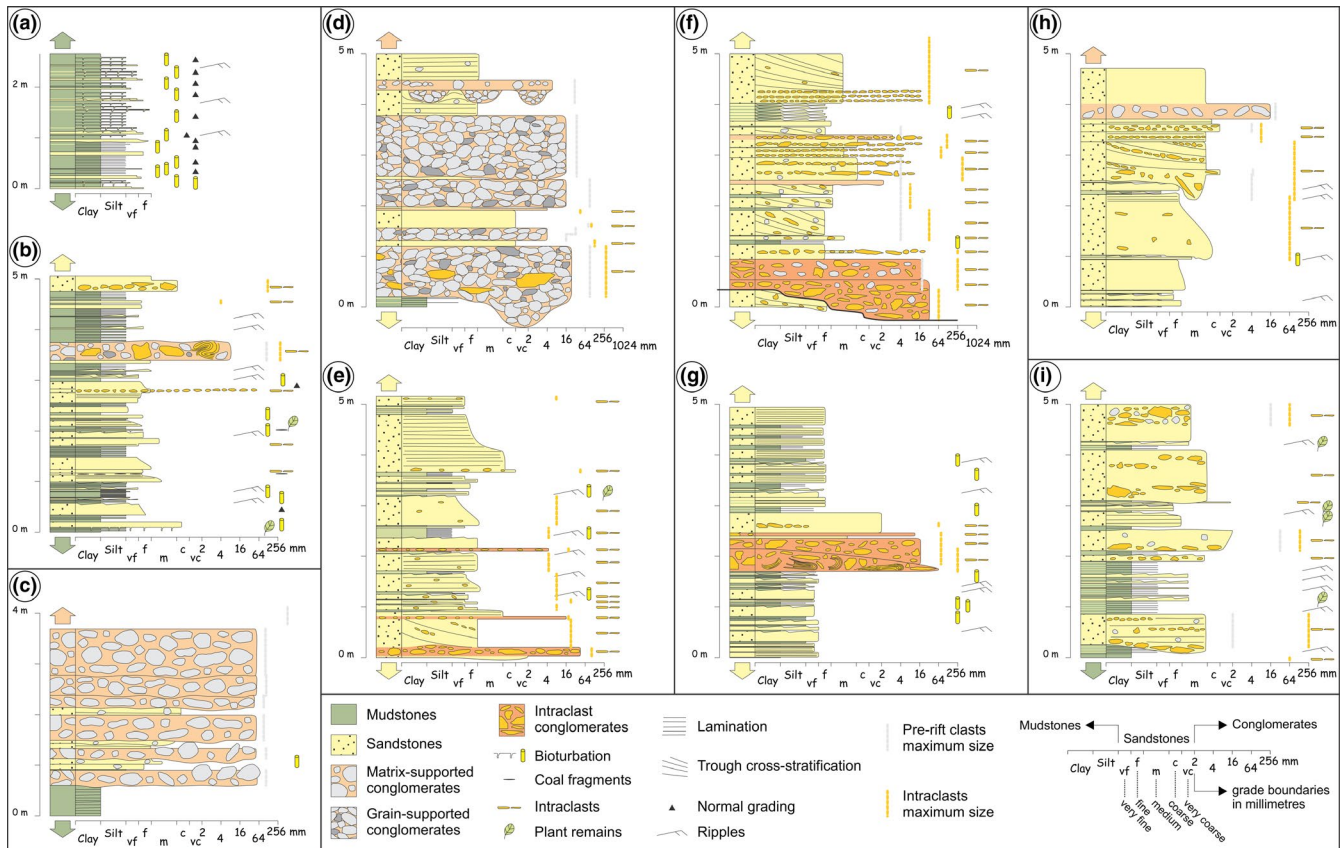


FIGURE 8 Representative sedimentary log sections for each type of depositional element (Figure 7). (a) and (b) Type A, mudstone-dominated sheets (a) and their sandstone enriched intervals (b). (c) Type B, conglomerate-dominated lobes. (d) and (e) Type C, conglomerate channel belts (d) and sandstone sheets (e). (f) and (g) Type D, sandstone channel belts: channel fill (f) and overbank deposits (g). (H) Type E, sandstone-dominated broad shallow lobes. (i) Type F, sandstone-dominated sheets with broad shallow channels. The UTM coordinates of the log sections are as follows: (a) 636,781 E, 4,213,508 N; (B) 638,733 E, 4,213,144 N; (C) 638,749 E, 4,213,236 N; (d) 638,730 E, 4,212,505 N; (e) 638,829 E, 4,212,376 N; (f) 638,823 E, 4,212,574 N; (g) 638,761 E, 4,212,529 N; (H) 638,819 E, 4,212,595 N; (I) 638,753 E, 4,213,159 N

moderately sorted lower coarse sandstone matrix. The clast fabric of the conglomerates is variable, ranging from chaotically orientated to more or less aligned parallel to the bedding and defining the stratification. The base of the conglomerate beds tends to be irregular and non-erosive, however, infrequent cases of conglomerate lenses with erosive bases occur. The sandstone lenses are finely laminated, down-cutting into previous sandstone lenses or draping the topography of the conglomerates below. These sandstones are moderately to well sorted, fine to medium in grain size and grain-supported.

The particular clast composition (Figures 5 and 7b) of the conglomerate-dominated lobes together with their isolated occurrence within the Type A mudstone-dominated sheets suggests a different origin than all other units in the area, sourced from local intrabasinal highs to the basin floor plain (Figures 1 and 5). The regular alternation in the stacking of conglomerate and sandstone beds in the lobes represents energy fluctuations in the subaqueous sediment density flows. Conglomerates were deposited from non-cohesive flows with intermediate characteristics between frictional laminar-flows

and semiplastic transitional flows (e.g. Sohn et al., 1997; Dasgupta, 2003; Sohn, 2000). Sandstones on the other hand, were deposited under more turbulent fluid flow conditions by non-channelized traction currents (e.g. Sohn et al., 1997; Dasgupta, 2003). The pervasive development of syn-sedimentary deformational structures throughout these deposits suggests their deposition over a soft unconsolidated substrate (i.e. type A units) that was subjected to dewatering by sediment loading.

6.3 | Type C - conglomerate channel belts and sandstone sheets (Unit 3)

This depositional element is found towards the base of the channel system and is more than 100 m thick (Figures 3 and 11). It consists of sand-rich intervals (80% sandstones and 20% mudstones) tens of metres thick, intercalated with conglomerate-dominated channel belts 5 to 20 m thick (Figures 7c and 11c). The proportion of conglomerates in the channel

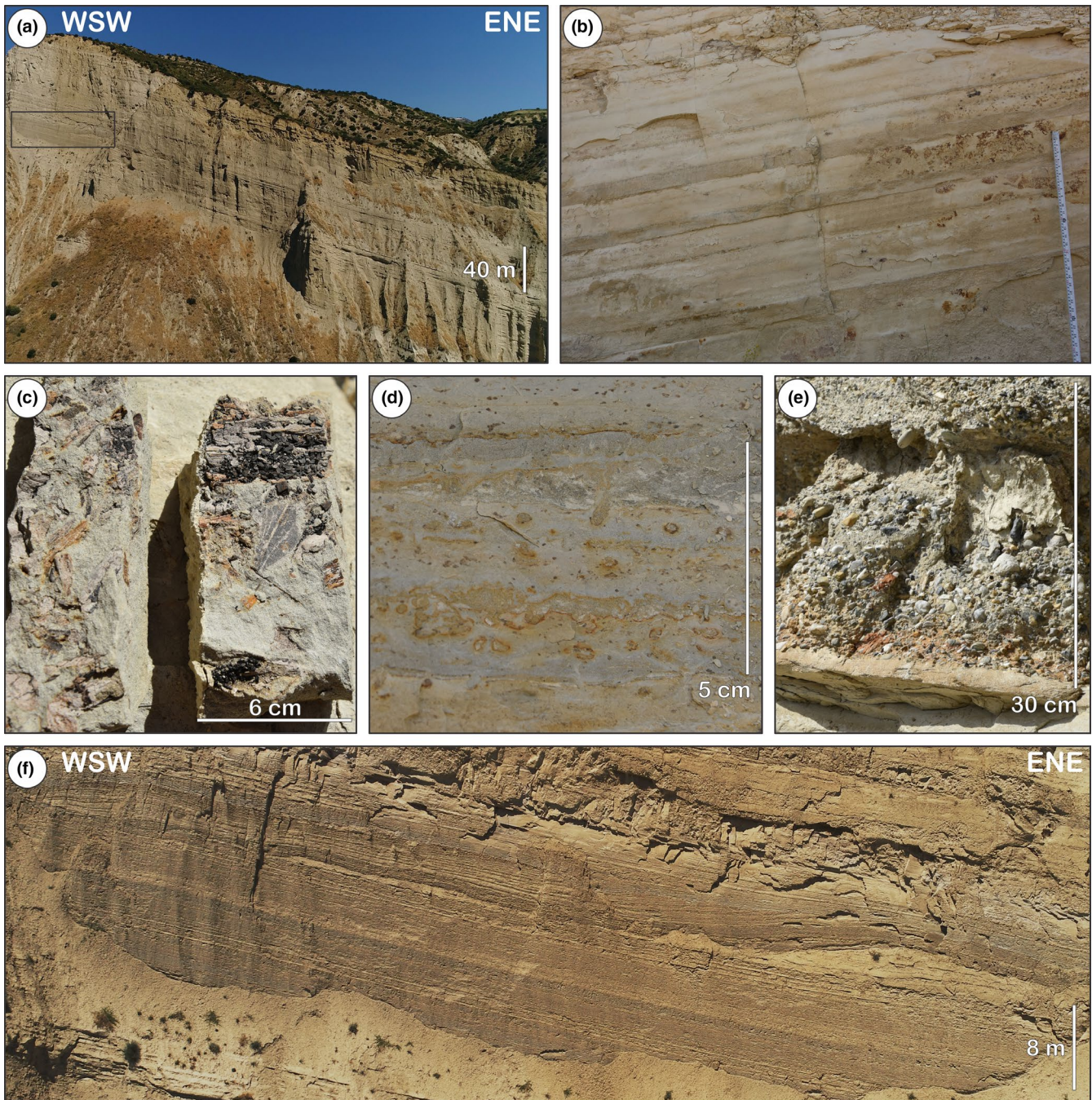
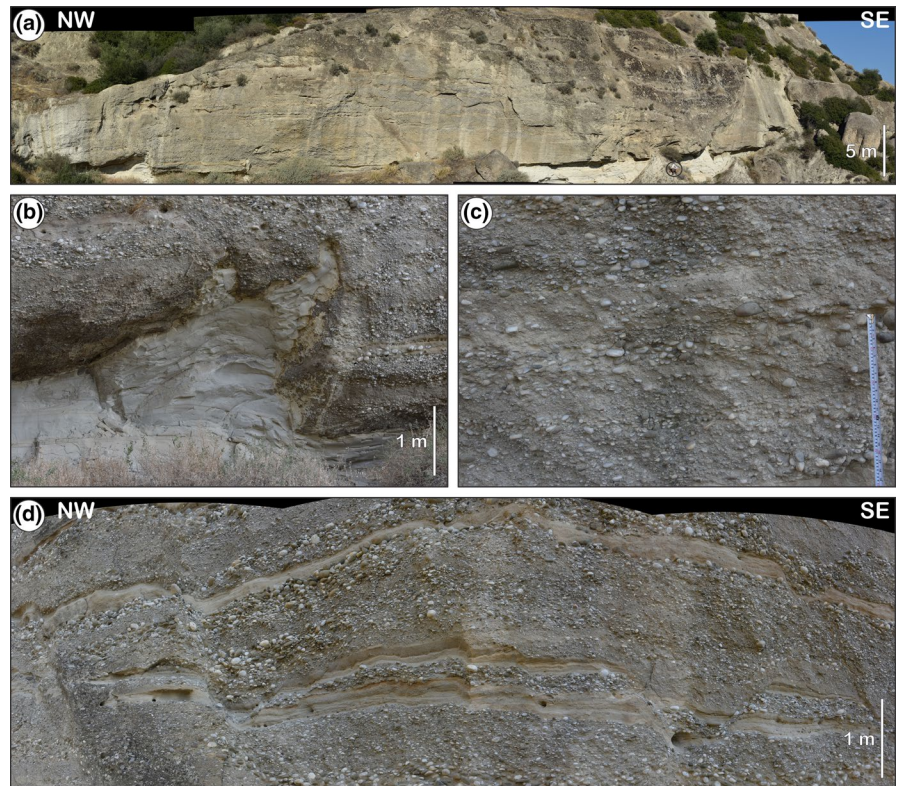


FIGURE 9 Field photographs of depositional unit type A. (a) Cliff exposures of alternating mudstone-dominated sheets in Unit 1. Intervals enriched in sandstone beds that appear intercalated can be laterally traced until they link with the exposures of the channel system (units 3, 7, 8 and 10; Figure 3). The black rectangle indicates the location of Figure 9f. (b) Centimetre-thick intercalations of tabular mudstones and sandstones. (c) Plant fragments at the base of the beds. (d) Bioturbation extending from the sandstone laminae into the mudstone intervals. (e) Conglomerate lens with 2–3 cm clasts supported in a fine to medium sandstone matrix. (f) Tapering wedges occur at the termination of the sandstone enriched intervals in Unit 1. These aggradational features are interpreted to represent the fringes of the internal units in the channel system (units 3, 7, 8 and 10; Figure 3) interdigitated with Unit 1. Field of view is approximately 100 m wide. The location of the wedge is indicated with a black rectangle in Figure 9a

belts is ~62%. The conglomerates are either tabular beds 0.2 to 1.2 m thick with irregularly flat bases, or erosive lenses 1 to 3 m thick that incise up to 2 m into underlying deposits (Figure 8d). These conglomerate bodies are grain- to matrix-supported and poorly sorted with diffuse horizontal

stratification, usually extending laterally for 10 to 40 m (Figure 12a and b). Planar cross-stratification is also present in a few cases, mainly restricted to the conglomerate lenses. The average grain size varies from 0.5 to 3 cm, with maximum sizes between 4 and 12 cm. Sandstone and mudstone

FIGURE 10 Field photographs of depositional element type B. (a) Lobate body with convex top and relatively flat base. Sitting person circled for scale. Field of view is approximately 100 m wide. (b) Marlstone dike injected at the base of the lobe in A. (c) Tabular matrix-supported conglomerate beds. Conglomerates are supported by a sandstone matrix. (d) Conglomerate beds 20 to 90 cm thick intercalated with 10–30 cm thick lenses of laminated fine to coarse sandstones subjected to intense soft-sediment normal faulting. Note that the highly irregular geometry of the bedding mimics the configuration of the small-scale faulting (grabens and halfgrabens) and neither channels nor scours are found among these conglomerates



intraclasts are especially frequent in these bodies in the lower half of the channel belts and span from 2 to 30 cm in length (Figure 12c). Lenses of laminated medium to coarse sandstones and granule-grade conglomerates are intercalated with the conglomerates in the channel belts.

External to the channel belts, 80% of the deposits are sandstones and 20% are mudstones (Figure 7c). These overbank deposits consist mainly of 0.5 to 1.2 m thick sandstone lenses intercalated with intervals composed of laminated and rippled 0.05 to 0.4 m thick tabular sandstone beds and centimetre thick massive or laminated mudstone and siltstone (Figure 8e). The sandstones in the thick lenses are fine to very coarse and variably poor to very well sorted (Figure 12d). They are frequently laminated, rarely cross-laminated and very often normal-graded with current ripples developed only at the top surface of the deposit (Figure 8e). They contain intraclasts typically 2 to 5 cm, but can be up to 20 cm long, floating within the bed or concentrated at specific levels. The tabular beds in contrast, are composed of well to very well sorted very fine to lower medium sandstones, with rare isolated intraclasts smaller than 2 cm.

Unit 3 shows interaction between high-energy channelized and mid- to low-energy non-channelized traction currents (e.g. Sohn et al., 1997; Dasgupta, 2003; Talling et al., 2012). The alternating conglomerate-dominated and sandstone-dominated intervals are therefore interpreted as a subaqueous migrating conglomeratic channel belt with finer-grained overbank deposits (e.g. Clark & Pickering, 1996; Janocko, Nemec, Henriksen, & Warchoř, 2013;

Posamentier & Kolla, 2003). The internal geometry of the channel belts, together with the presence of sandstone lenses between the conglomerate bodies, show that the channel belts were filled by multiple depositional events from subaqueous sediment density flows of variable energy. The deposition of a dominantly conglomerate fraction in the channel belts is interpreted as an evidence for bypassing of the finer-grained fractions of sediment down-system (e.g. Hubbard, Covault, Fildani, & Romans, 2014; Li, Kneller, Hansen, & Kane, 2016; Stevenson, Jackson, Hodgson, Hubbard, & Eggenhuisen, 2015). The concentration of sandstone and mudstone intraclasts towards the lower half of the channel belts reflects erosion of the overbank deposits during initial excavation of the channel belt.

6.4 | Type D - sandstone channel belts (Unit 7)

Unit 7 is the second depositional unit in the channel system and is characterized by the development of a 17 m thick channel belt towards the top of the unit that extends laterally for more than 300 m (Figures 3, 7d, 11a, b and d). The channel belt deposits are predominantly composed by sandstones (81%), with a smaller contribution of mudstones (9 to 16%), conglomerates (up to 2.5%) and intraclast conglomerates (up to 8%). In contrast, the overbank deposits have a smaller representation of sandstones (64%) and higher proportion of mudstones (29%) with intraclast conglomerates in some cases

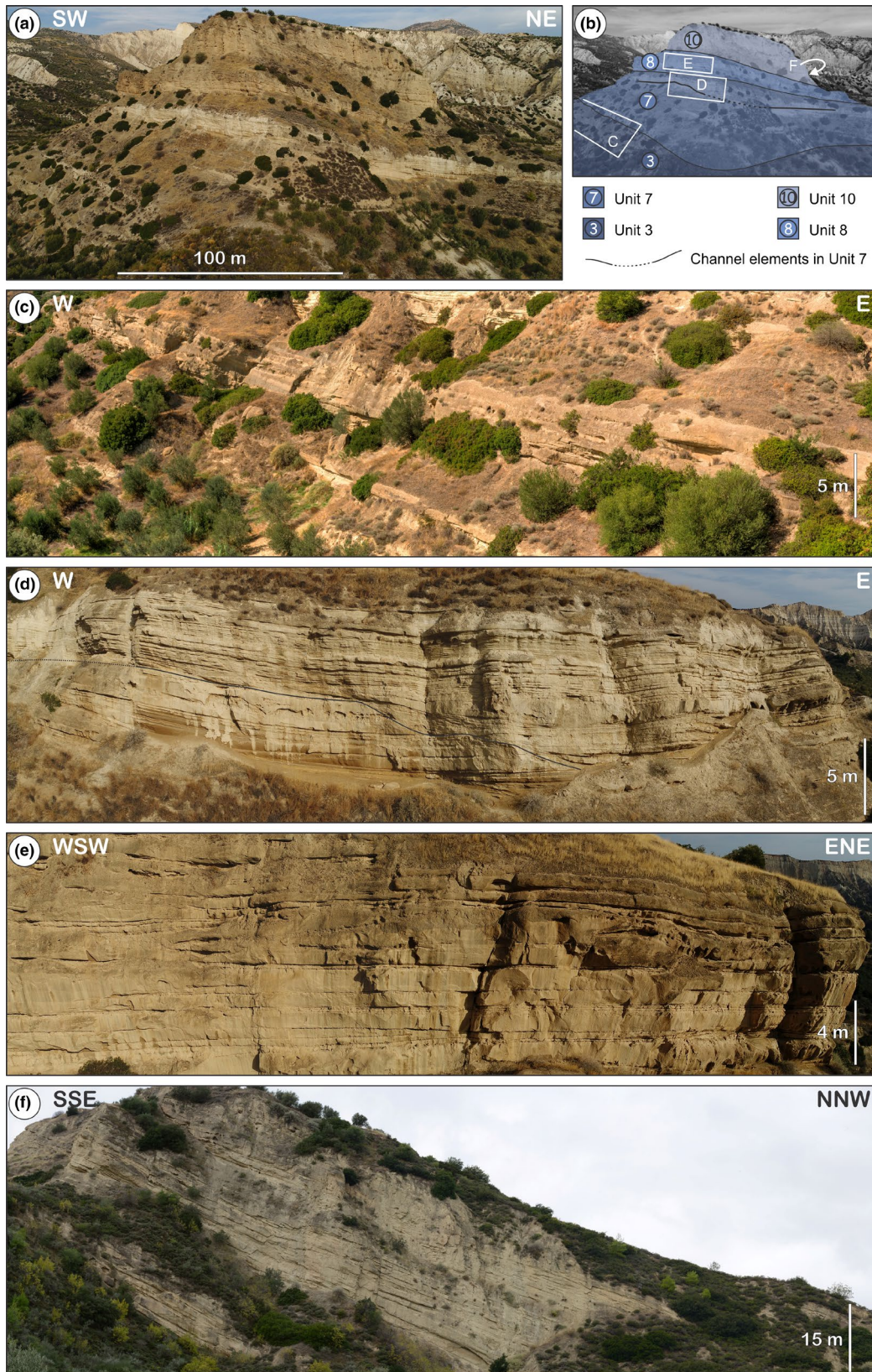


FIGURE 11 Field photographs of the channel system exposed at the Riza hill (Figure 2a). (a) Aerial view of the Riza hill. (b) Distribution of the internal units in the channel system (units 3, 7, 8 and 10; Figure 3) and their boundaries. White rectangles indicate the relative location of the pictures in c, d, e and f. (c) Depositional element type C: conglomerate-dominated channel belts in Unit 3. (d) Depositional element type D: southwestern margin of a channel element in Unit 7. (e) Depositional element type E: sandstone-dominated lobe in Unit 8. (f) Depositional element type F deposits: sandstone-dominated succession with shallow channels in Unit 10

(up to 7%). Individual channel elements in the belt are up to 12 m thick and 140 m wide. The channel fill is composed of very broad sandstone lenses 0.3 to 1.4 m thick, intercalated with up to 50 cm thick intervals of mudstones and tabular rippled and laminated well sorted very fine to medium sandstones and siltstones (Figure 8f). The stratal geometry within each channel defines large-scale low-angle trough cross stratification, given by the gradual thickening of the sandstone lenses towards the middle of the troughs and thinning away until pinching out against the margins of the channels (Figure 11d). The sandstone lenses are also observed to onlap onto the top of the channel banks once the channel depressions become filled. Intraclast conglomerates (Figures 8f, 12e, f) are found both as flat-lying lenses at the base of the channels and as wedges accreted to the lateral margins of the channel (Figure 11d). These lateral wedges onlap the channel margins and downlap progressively and asymptotically onto the channel base away from the margins, thinning towards the thalweg of the channel (Figure 11d). Channelization does not appear to follow any particular vertical pattern. The different scales of channelization observed (lenses, troughs and channel elements) within the channel belts are evenly distributed laterally giving way to the development of multiple internal erosional surfaces. The broad sandstone lenses are planar or cross laminated, well sorted and medium to coarse-grained, with intraclasts 1 to 15 cm long, floating or aligned along the stratification. Pebble lags are common at the base of the channel elements. The deposits external to the channel belt are composed mostly of well sorted fine to very fine tabular sandstone beds, 5 to 40 cm thick, with planar lamination and ripples at the top. These sandstone beds are interbedded with centimetre-thick structureless or laminated mudstones and rippled siltstones and very fine sandstones (Figures 8g and 12g).

This channel belt resulted from the migration and erosion of a series of trunk channels through overbank deposits in a subaqueous environment dominated by sediment density flows (e.g. Clark & Pickering, 1996; Janocko et al., 2013; Posamentier & Kolla, 2003). Deposition inside and outside the channels was essentially similar, consisting of episodic deposition of sand by traction currents separated by thin mudstones denoting pauses and suspension fallout (e.g. Dasgupta, 2003; Talling et al., 2012). The overall coarser size of the sandstones in the channel fill (Figure 8f) indicates that deposition in the channels occurred at higher energy levels than those recorded by the overbank deposits (Figure 8g). Similarly, the presence of lithic pebble lags in the channels (Figure 8f) suggests that the processes responsible for the channel cuttings were more energetic than those that led to the filling of these erosive features with predominantly sandstone deposits. The composite nature of the channel belt together with the pebble lag deposits and wedges of intraclast conglomerates at the base and margins of the channel elements indicate bypassing of sediment down-system (e.g.

Hubbard et al., 2014; Li et al., 2016; Stevenson et al., 2015). Similarly, the alternation of thick sandstone lenses and thinner-bedded and finer-grained intervals that characterize the channel fill indicates the existence of multiple discrete depositional events during the lifetime of each channel element (e.g. Hubbard et al., 2014; Li et al., 2016; Stevenson et al., 2015). The wedges of intraclast conglomerates in the overbank deposits (Figure 8g) are interpreted to originate from the burst and collapse of the channel levees and deposition of crevasse-splays.

6.5 | Type E—sandstone-dominated broad shallow lobes (Unit 8)

This unit is sandstone-dominated (94%) with a minor amount of conglomerates (5%) and mudstones (1%) (Figure 7e). It is characterized by the development of thick lensoidal beds (60 to 140 cm thick) of moderately sorted medium to very coarse sandstones that are continuous for hundreds of metres (Figure 11a, b and d). The base of these lenses can be locally highly erosive, but also extending flatly for tens of metres. Although there is a tendency for the tops to be generally flat, it is not uncommon to find lenses with gently convex tops. The conglomerates have grains 1 to 3 cm long supported in a moderately sorted medium sandstone matrix. They constitute 0.3 to 1 m thick bodies transitional at the base of the sandstone beds or also found as individual erosive lenses (Figure 8h). The stacking of sandstone and conglomerate lenses defines, in some places, lobate bodies with distinctive convex tops that taper laterally from 4 m to 1 m thick over a horizontal distance in the order of 50 m (Figure 8h). Due to the variable nature of the bases of the sandstone and conglomerate bodies the lobes also can develop erosive bases (Figure 12h). Finer-grained deposits such as mudstones and very fine to fine rippled sandstones appear intercalated between the thick sandstone and conglomerate lenses in intervals less than 30 cm thick (Figure 12i).

The characteristic rock-body geometry of Unit 8 together with the predominance of thick bedded sandstone beds are typical features of subaqueous sediment density flow lobe complexes, consisting of stacked and partially amalgamated lobe elements (e.g. Pr lat & Hodgson, 2013; Pr lat et al., 2009). Thick sandstone beds are interpreted to have been deposited by progressive aggradation from high-density sediment flows (e.g. Kneller & Branney, 1995; Talling et al., 2012). The erosive nature of the basal boundaries of some sandstone beds, conglomerate lenses and lobe elements indicates sediment bypassing (e.g. Stevenson et al., 2015), which is often associated to a proximal position in the lobe setting, close to the channel-lobe transition (e.g. Brooks et al., 2018; Normark, Piper, & Hess, 1979; Pemberton, Hubbard, Fildani, Romans, & Stright, 2016; Wynn et al., 2002).

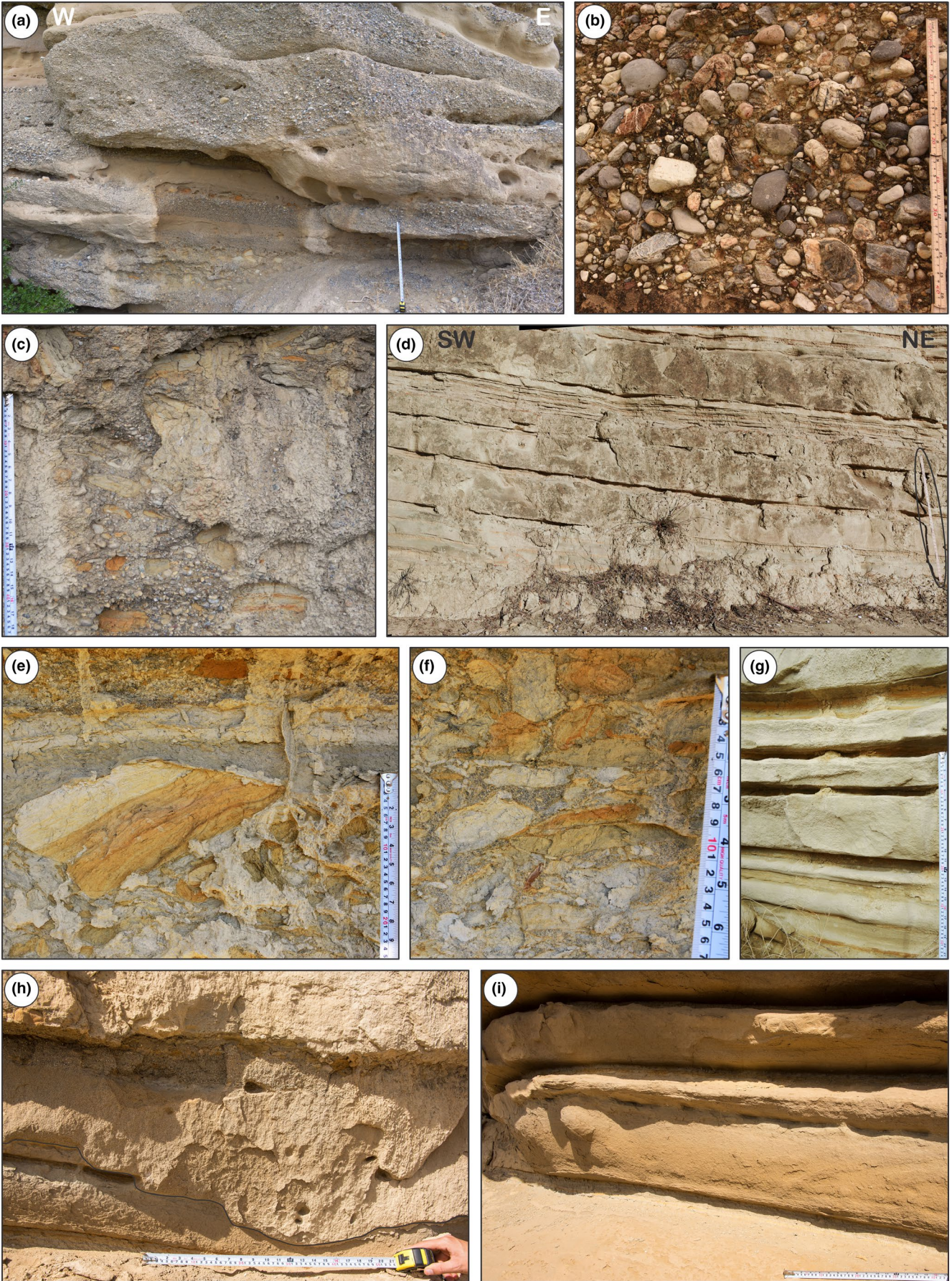


FIGURE 12 Field photographs of depositional element type C (a, b, c and d), type D (e, f and g) and type E (h and i). (a) Tabular conglomerate beds intercalated with laminated sandstones. (B) Poorly sorted grain- to matrix-supported conglomerate with sandstone matrix. (c) Conglomerates rich in sandstone and mudstone intraclasts (2–30 cm in length) in deposits at the lower half of a channel belt. (d) Decimetre thick sandstone beds intercalating thinner, centimetre thick, rippled sandstones and mudstones found external to the channel belts. Ruler (circled) on the right-hand side is 1 m in length. (e and f) Concentration of intraclasts at the margins of a channel element in Unit 7 (depositional element type D). (g) Deposits external to the channel belts in Unit 7 (depositional element type d). Tabular sandstone beds with ripples on top interbedded with laminated mudstones and rippled siltstones. (h) Evidence of erosion at the base of a body of coarse to very coarse sandstones and fine pebble-grade conglomerates. (i) Fine to medium sandstone beds 15 to 30 cm thick intercalated with 2 to 5 cm thick intervals of mudstones and very fine rippled sandstones

6.6 | Type F—sandstone-dominated sheets with broad shallow channels (Units 10, 13 And 16)

These units are exposed as sandstone-dominated sheets 30 to 65 m thick, extending laterally for more than 3.5 km (Figure 7f). Type F units are found at the top of the channel system (Unit 10) or above the $\sim 6^\circ$ unconformity (units 13 and 16) intercalated with Type A mudstone-dominated units 11 and 14 (Figures 3, 11a, b, f and 13a). Sandstone content ranges from 63% to 87% with conglomerates accounting for 16 to 25% and mudstones representing 9 to 19% of the thickness of the sheets. The deposits are mostly composed of laterally elongated sandstone channels (46 to 66%), 0.3 to 4 m thick and up to 70 m wide (Figure 13c). Their grain size varies from medium to very coarse sand, typically containing floating mudstone and sandstone intraclasts 1 to 13 cm in length that can reach maximum sizes of 26 to 50 cm (Figure 8i). The sandstone channels are diffusely laminated or stratified with sharp erosive concave to subplanar bases. Conglomerates are usually found at the base of the sandstone channel bodies as amalgamated laminated and stratified grain-supported moderately to well-sorted lenses (Figure 13d). More rarely, the conglomerates occur as isolated tabular beds 0.5 to 2 m thick in which clasts are supported by a fine to coarse sandstone matrix. Grain size varies from 0.2 to 5 cm in average and maximum of 15 cm. Mudstone and sandstone intraclasts are also present in the conglomerate bodies. The sandstone and conglomerate bodies intercalate 0.2 to 1.2 m thick intervals of centimetric tabular beds of mudstones and rippled siltstones and very fine to medium sandstones (Figure 13b). Tabular bodies, 1 to 3 m thick, composed of intensively sheared and folded mudstone and sandstone intraclasts also occur in the deposits corresponding to Unit 13. Intraclasts are up to 150 cm long and supported in a chaotic mudstone-rich matrix with occasional floating granules and pebbles. The orientation of the intraclasts is generally random and only the largest and most elongated tend to align subparallel to the bedding (Figure 13e).

The great lateral extent of Type F units, their sheet geometry and the abundance of broad shallow channels allow for its interpretation as a subaqueous sediment density flow distributary fan setting (e.g. Hodgson et al., 2006; Oluboyo, Gawthorpe, Bakke, & Hadler-Jacobsen, 2014; Posamentier & Kolla, 2003). The geometry of the channels and their deposits indicate shallow erosion by traction currents and bypassing of sediment

down-system before being filled by progressive aggradation from high-density sediment flows (e.g. Kneller & Branney, 1995; Talling et al., 2012). The rippled thin-bedded sandstones and siltstones in the overbank intervals are interpreted as deposits from unconfined turbulent flows, low-density turbidity currents (e.g. Dasgupta, 2003; Talling et al., 2012), whereas the mudstones represent deposition from suspension fallout (e.g. Dasgupta, 2003; Talling et al., 2012). The intraclast conglomerates among the overbank intervals are interpreted as debris flow deposits (e.g. Dasgupta, 2003; Sohn, 2000; Sohn et al., 1997) that originated from the gravitational instability of unconsolidated deposits, as is demonstrated by the soft-sediment deformational features observed in the intraclasts.

7 | SLIDE SHEETS

The stratigraphically youngest RDF exposures in the northern part of the Amphithea fault block show a succession of slide sheets stacked in a complex that exceeds 200 m of thickness (Figures 2a, b, 3 and 14). Dip sections of the slide sheets are well exposed along vertical cliffs on the margins of the SE to NE orientated drainage network (Figure 2a), but strike sections are not so well developed and tend to be covered in vegetation. Only the frontal and posterior ends of the slide sheets are thus exposed and no lateral terminations or structures such as tear faults can be observed. The individual slide sheets contain mainly portions of Unit 16, thrust along slices of Unit 14, ranging in thickness from 10 to 30 m (occasionally up to 70 m) and dipping more steeply than the units in the RDF exposed immediately to the south (Figure 2a, b). Mapping of the individual slide sheets is limited by the extent of the outcrops, ranging from 200 to more than 500 m in both dip and strike direction. Thrust ramp and flat geometries can be identified and strike predominantly northwest-southeast (Figure 14c) and have a northeast sense of vergence (Figure 14d). This strike orientation is parallel to that of the north and south boundary fault systems of the Amphithea fault block and is oblique to internal normal faults (Figures 1, 2a, b and 14e).

Subaqueous translational and rotational slides (or slumps) happen in a wide range of slopes, from as shallow as $<1^\circ$ to very steep scarps (e.g. Bull, Cartwright, & Huuse, 2009; Lewis, 1971; Moernaut & de Batist, 2011). The occurrence of thrust slide sheets tend to develop towards the lower reaches

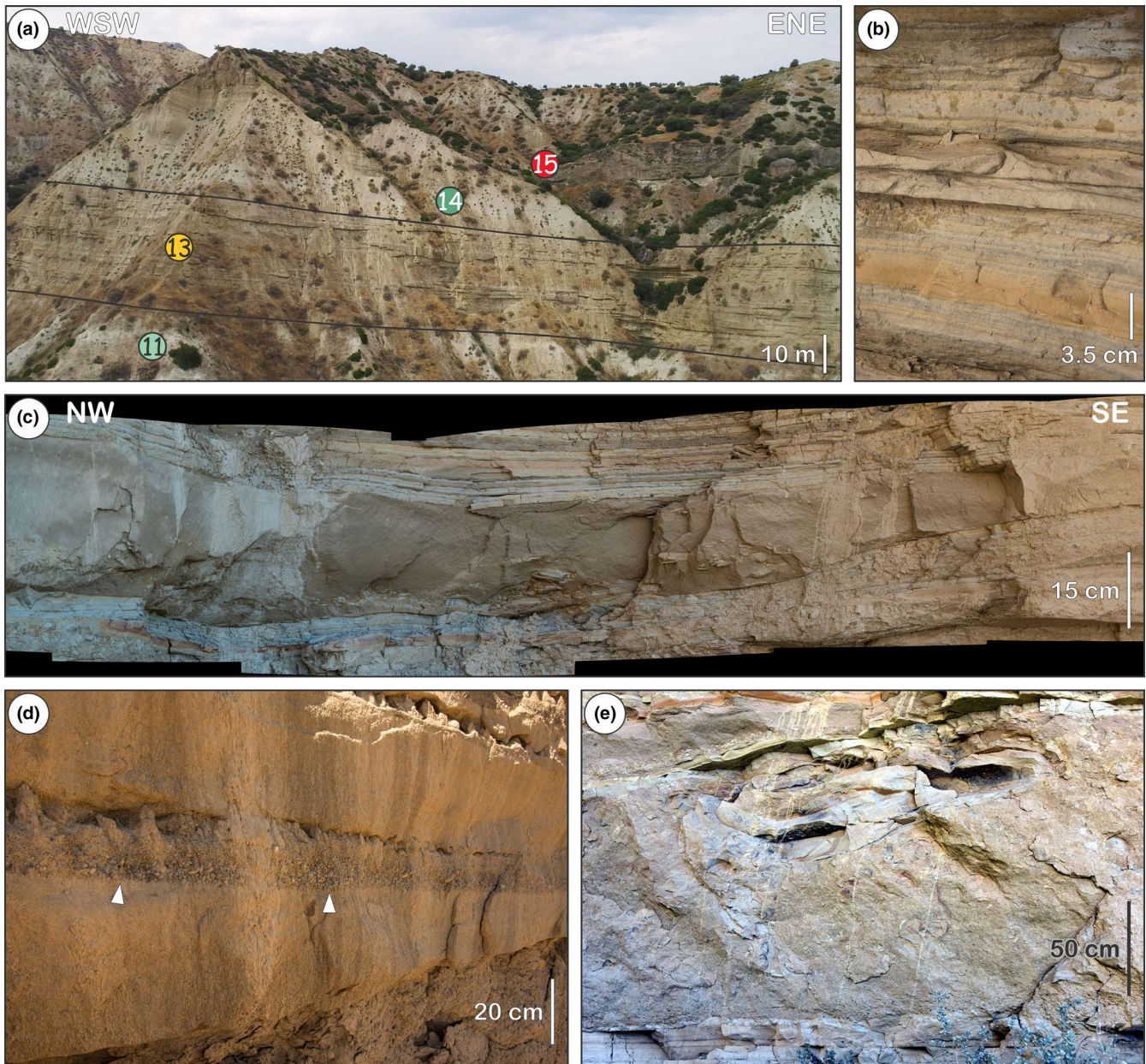


FIGURE 13 Depositional element type F. (a) Aerial view of Unit 13. Coloured circles indicate the different units in the cliff section (Figure 3). (b) Rippled siltstones and sandstones intercalated with marlstone laminae. (c) Typical sandstone channel containing sandstone and mudstone intraclasts. (d) Two vertically amalgamated sandstone lenses. A grain-supported conglomerate is found at the base of the upper lens (indicated with white arrows). (e) Unrooted isoclinally folded sandstone intraclast towards the top of a mudstone-supported tabular deposit towards the base of Unit 13

of the slope (toes), where the slides arrest (e.g. Lewis, 1971; Frey Martinez, Cartwright, & Hall, 2005; Frey Martinez, Cartwright, & James, 2006; Bull et al., 2009; Moernaut & de Batist, 2011). The fact that the slide complex exceeds 200 m in thickness implies at least a similar throw in the northern boundary fault system in order to accommodate such a stacking of slide sheets. This magnitude of fault throw could not be achieved without the consequent tilting of the Amphithea hangingwall towards the NNE. The slide sheets are thus interpreted to have originated as a result of the tilting of the hangingwall block towards the NNE after deposition of Unit 16 (Figures 2a, b, 3 and 14). The strong lithological contrast between

mudstone-dominated Unit 14 and sandstone-dominated Unit 16 encouraged development of detachments towards the upper part of Unit 14 (Figure 14f). These detachments allowed slices of units 14 and 16 to slide, following the hangingwall palaeoslope towards the northeast, stacking one on top of the other against the northern margin of the Amphithea fault block (Figure 14g). It remains unclear, however, whether the triggering and downslope slide of these sheets occurred as one major subaqueous landslide or rather as a series of gravitational instability events spaced through time. Similarly, the relative duration of the landslide/s cannot be constrained. Presence of tight sheath folding and *boudinage* at basal detachment zones

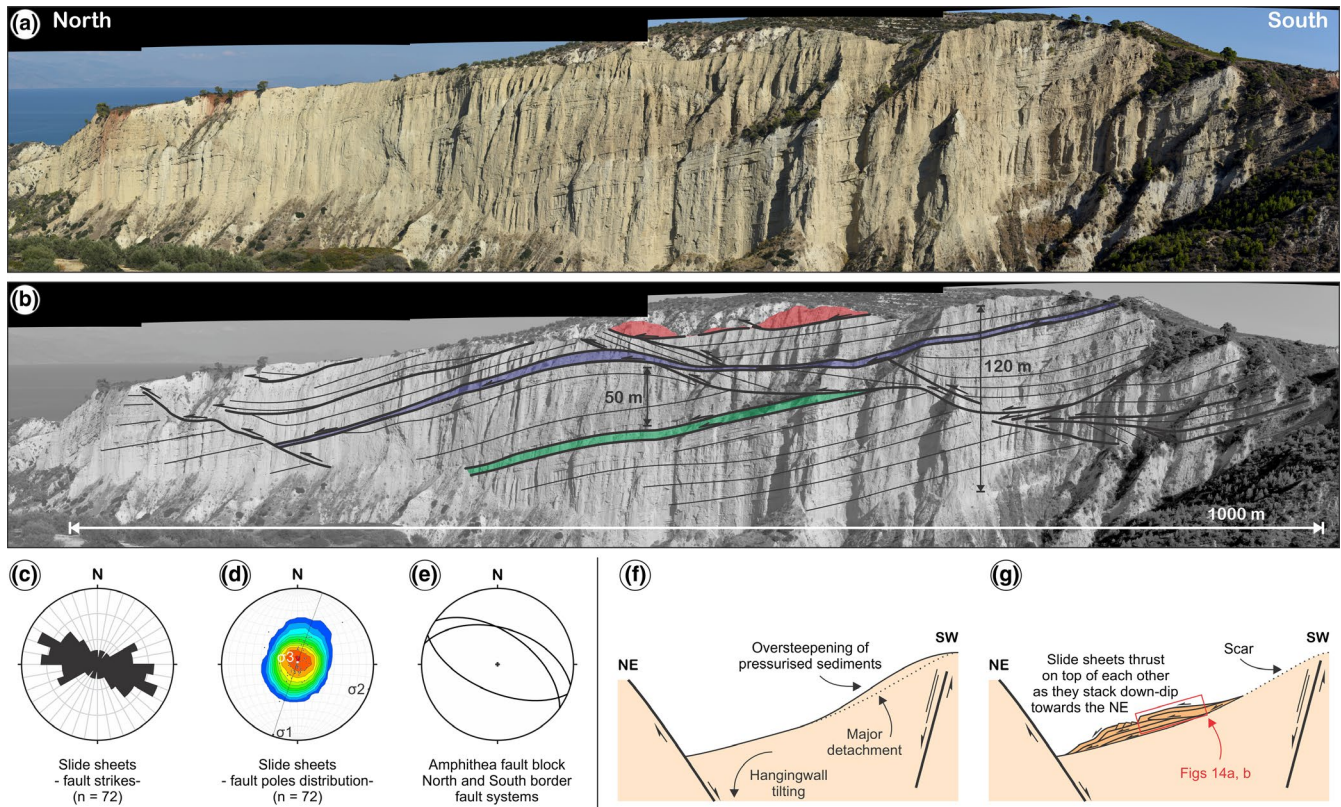


FIGURE 14 Slide sheets towards the top of the RDF in the Amphithea fault block (Figures 2 and 3). Vergence of the thrust slide sheets is towards northeast. (a) Field photograph and line interpretation (b). Selected marker intervals are indicated with green, blue and red colours. Pictures in (a) and (b) taken from 639,109 E, 4,214,709 N. The orientation of the fault ramps and flats in the thrust sheets was measured from the digital outcrop models from LiDAR and photogrammetry and restored according to the Amphithea fault block regional dip and dip direction: (c) rose diagram of fault strike and (d) fault plane poles density distribution and its principal stresses orientation (σ_1 : maximum, σ_2 : intermediate and σ_3 : minimum). Note that the strike of the thrusts parallels that of the northern and southern fault boundary systems in the Amphithea fault block (e) (Figures 1 and 2). (f) and (g) Sketches illustrating the development of the slide sheets in the Amphithea fault block. (g) Continuous tilting of the hangingwall towards the NE led to oversteepening of overpressurized deposits in units 14 and 16. Major and minor detachments were thus generated, over which sheets slid to the NE, following the topographic gradient (g). Stacking of the slide sheets resulted in their thrusting with a NE vergence. Note that the diagrams in (f) and (g) are not to scale and proportions are exaggerated for better visualization

in slides is often attributed to creep (e.g. Lucente & Pini, 2003). None of these structures are observed for the present case; however, the sharp thrusts developed instead, may reflect mainly the contrasting competence of the lithologies involved with no implications for the duration of the slides.

8 | DISCUSSION

8.1 | Sedimentary and tectonic evolution of the Rethi-Dendro Formation in the Amphithea fault block

The sedimentary analysis of the depositional elements and the different stratigraphic units allows a better understanding of the evolution of the lacustrine deep-water environment of the RDF. In particular, the recognition of angular unconformities within the stratigraphic units is used to identify major phases of hangingwall tilting and their control on the subaqueous

environments (e.g. Ravnås & Steel, 1997; Muravchik et al., 2018). The clast composition of the RDF in the Amphithea fault block remains unchanged during its evolution, indicating more-or-less fixed sediment sources. However, large changes in palaeotransport direction are observed across the $\sim 6^\circ$ unconformity which are analysed below in terms of the structural configuration of the Amphithea fault block and its tectonic context in the Corinth Rift. The link between the sedimentary evolution of the RDF to changes in lake/marine level or climate is difficult to constrain, but possible scenarios are discussed.

8.1.1 | Deposition below the $\sim 6^\circ$ angular unconformity

Below the $\sim 6^\circ$ angular unconformity (Figure 15a, b, c), the Amphithea fault block had a halfgraben configuration defined by the Koutsa and Melissi faults towards the north-west and north and the Amphithea fault at the southern

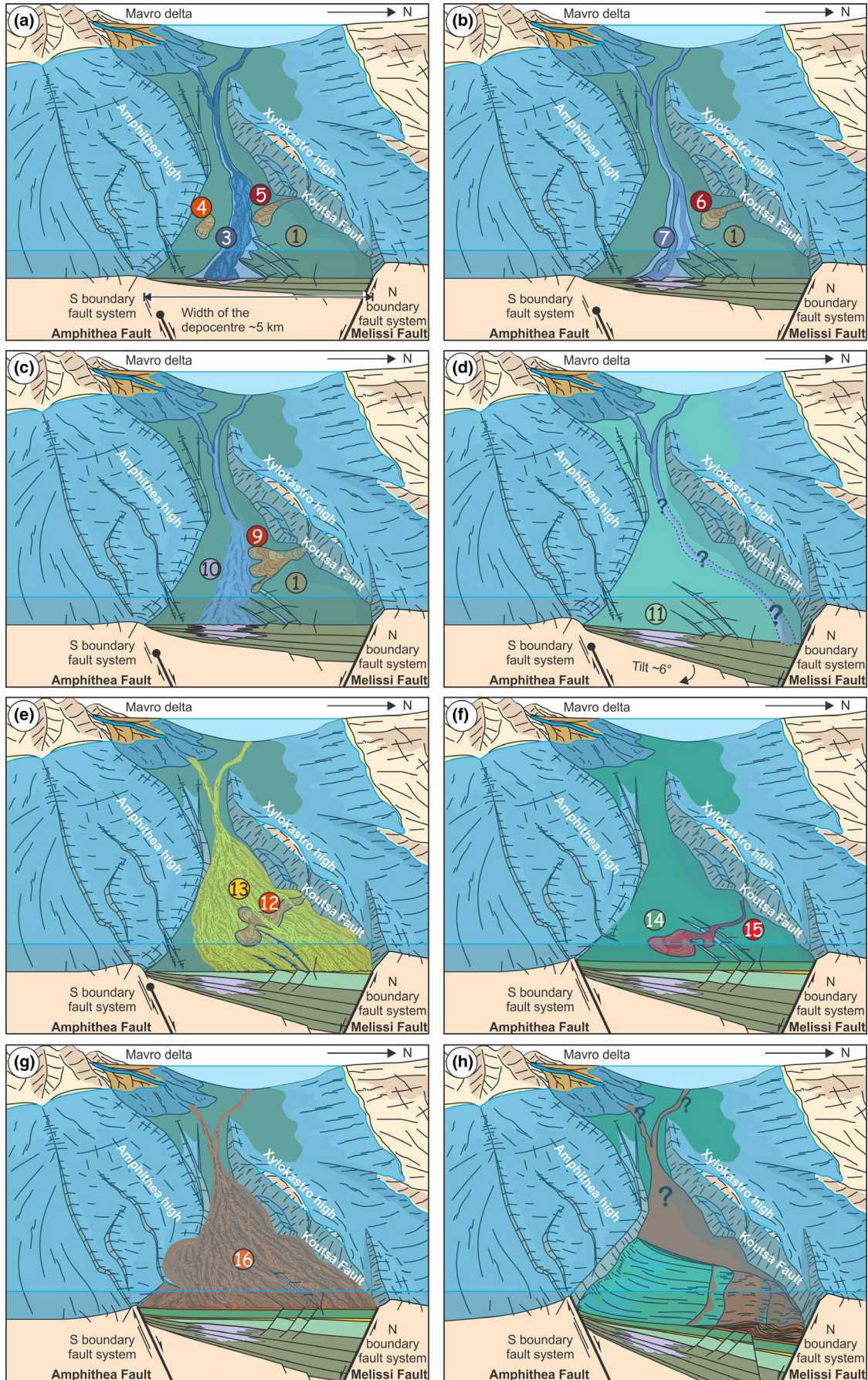


FIGURE 15 Tectono-sedimentary models of the evolution of the RDF depositional environment in the Amphithea fault block. View towards the west. Representation of the northern margin of the basin is schematic and only for illustrative purposes. Numbered coloured circles correspond to the different stratigraphic units identified in this study (Figures 2 and 3). Base level (lake/marine) is kept constant throughout the models. (a, b and c) Deposition below the $\sim 6^\circ$ angular unconformity. Development of an axial channel system (units 3, 7, 8 and 10) fed from the Mavro delta and funnelled between the Amphithea and Xylokaastro highs on a basin floor plain (Unit 1). Subordinately, a transverse system consisting of conglomerate-dominated lobes (units 2, 4, 5, 6, 9) is sourced from the Xylokaastro high. Different stages in the evolution of the channel system are illustrated for the deposition of conglomerate channel belts and sandstone sheets (a), sandstone channel belts (b) and sandstone-dominated sheets with broad shallow channels (d). (b) Tilting of the Amphithea hangingwall block towards the NNE occurs from a combination of the accrued displacement in the northern border and the growing faults at the southern border. Fine-grained deposition becomes dominant (Unit 11). There are presently no evidences that any channel system such as the one in (a) existed for this stage. Nevertheless, it is possible that the channel system migrated closer to the northern fault border following the north-eastwards basin floor gradient caused by the tilting of the hangingwall and its deposits lie present-day in the subsurface. (c) Deposition of a sandstone-dominated sheet with broad shallow channels (Unit 13) sourced from the Mavro delta and conglomerate-dominated lobes (Unit 12) sourced from the Xylokaastro high. (d) A new phase of fine grained deposition (Unit 14) dominates the Amphithea hangingwall. Occasionally, conglomerate-dominated lobes (Unit 15) sourced from the Xylokaastro high reach the basin floor. (e) Renewed deposition of a sandstone-dominated sheet with broad shallow channels (Unit 16) sourced from the Mavro delta. (f) Continuous tilting of the Amphithea fault block generated gravitational instabilities that triggered large-scale landslides containing sheets of units 14 and 16. These slide sheets thrust each other as they moved downslope and stacked in a complex of NE vergence on the northern half of the depocentre. The palaeotransport direction of the channel system below the $\sim 6^\circ$ angular unconformity (a, b and c) is towards the SE, perpendicular to the internal faults in the Amphithea fault block (Figure 6b), whereas for the units above that unconformity (b, c, d and e) their palaeotransport directions are orientated towards the NE, parallel to the strike of these internal faults (Figure 6c)

margin (Gawthorpe, Leeder, et al., 2017). The RDF was characterized by a mudstone-dominated succession (Unit 1) and a channel system (units 3, 7, 8 and 10) sourced from the Mavro delta and conglomerate-dominated lobes derived from the Xylokaastro high (units 2, 4, 5, 6, 9). The channel system displays an overall change in depositional style from channel complexes in the lower half (units 3 and 7) to lobe complexes in the upper half (units 8 and 10), denoting a clear retrogradational pattern. Similarly, the coarser grain-sizes are mainly concentrated in the basal Unit 3. Although conglomerates are sparsely developed throughout all the channel system units, it is only in Unit 3 that conglomerate beds are fully developed and clast sizes reach dimensions comparable to those found in the Mavro delta (Rohais et al., 2007). Retrogradation of deep-water channel systems is a typical processes that can be ascribed to autocyclicality of the depositional system or due to variations in the base level (sea/lake) (e.g. Brooks et al., 2018; Normark et al., 1979; Pemberton et al., 2016; Posamentier & Kolla, 2003; Wynn et al., 2002). In this particular case, its exact origin cannot be established from the data collected. No clear indication of tectonic controls in the Amphithea fault block on this retrogradation have been found, apart from the $\sim 8^\circ$ angular unconformity immediately below the channel system exposures in Fault Block 1. However, the reduced level of exposure of this structure prevents any attempt of linking its presence with the evolution of the channel system.

The tilting of the hangingwall was towards the north-east, whereas the orientation of the channel system was NW-SE with flow towards the southeast, parallel to the fault-controlled margins of the Amphithea fault block and perpendicular to the internal faults in the depocentre

(Figures 6b, 15a). The channel system is interpreted to have been diverted to the southeast by the down-stepping internal faults, once it emerged from the constriction between the Amphithea and Xylokaastro highs and entered the Amphithea hangingwall block (Figure 15a). The thickest channel system deposits (at Riza hill) lie in close proximity to the axis of the synformal monocline flexure that runs parallel to and in the hangingwall of the Amphithea fault (Figure 2a). This present-day flexure originated in front of a steepening monocline limb developed above the growing, but blind Amphithea fault (Figures 4a, b, c and 15a, b, c). The location and orientation of the channel system is thus interpreted to have been controlled by the position of these coupled positive and negative topographic features (e.g. Kane, Catterall, McCaffrey, & Martinsen, 2010) in conjunction with the gradients caused by the internal faults.

8.1.2 | Development of the $\sim 6^\circ$ angular unconformity

The $\sim 6^\circ$ angular unconformity results from the tilting of the Amphithea hangingwall towards the NNE as a result of displacement on the S-dipping Melissi fault along the northern margin of the depocentre (Figure 15b). Such magnitude of tilting implies a throw of at least 500 m on the northern boundary system for a halfgraben with the dimensions of the Amphithea fault block. This generated enough accommodation that mudstone became the dominant sediment accumulating in the hangingwall (Unit 11, Figure 15d). The channel system as a whole, is interpreted to have migrated closer to the northern boundary fault system due to ground tilting (e.g. Kane et al., 2010).

However, this hypothesis cannot be tested because only higher levels of the stratigraphy are currently exposed.

8.1.3 | Deposition above the ~6° angular unconformity

The stratigraphy above the ~6° angular unconformity alternates between mudstone-dominated sheets (units 11 and 14; Figure 15d and 15f) and sandstone-dominated sheets with broad shallow channels (units 13 and 16; Figure 15e and 15g), with intercalations of conglomerate-dominated lobes sourced from the Xylokaastro high (units 12 and 15; Figure 15e and 15f). Palaeotransport directions measured in deposits sourced from the Mavro delta (units 11, 13, 14 and 16) are predominantly towards the northeast, orientated subparallel to the internal faults within the Amphithea hangingwall (Figure 6c). This is interpreted to reflect the persistence throughout these stratigraphic units of a basin floor topographic gradient towards the S-dipping fault boundary (Melissi fault) in the northern margin of the Amphithea fault block. However, the conformable nature of units above the ~6° angular unconformity indicates that the changes in the depositional system (alternating mudstone and sandstone-dominated units) are not directly related to hangingwall tilting events in the Amphithea hangingwall that could have re-routed the supply of sediment away from this sector of the basin. This alternation was probably controlled by processes external to the depositional setting: for example tectonics in the source area, climatic modulation, variations in base level of the water body (lake/sea) or autocyclicality of the deltaic feeder system. The Mavro delta is interpreted to have a dominant northwards progradation direction and radial distribution of palaeocurrents (Rohais et al., 2007), so its sourcing to the Amphithea fault block could have been subjected to autocyclic shifting of the delta lobes, leading to periods of reduced delivery of sand and coarser sediment to the depocentre and development of the thick accumulations of mudstone-dominated units 11 and 14.

8.1.4 | Large-scale subaqueous landslide

The thick succession of slide sheets found at the top of the RDF in the area (Figures 2a, b, and 14) represents the end of the Amphithea hangingwall as an effective sediment fairway to deeper and more distal regions in the basin to the east (Figure 15h). The triggering of this large-scale subaqueous slide complex is interpreted to be due to tectonic activity on the faults bounding the southern and northern margin of the Amphithea fault block and associated to the tilting of the hangingwall towards the NNE. The fact that

the slide complex is overlain by the Pleistocene Kryoneri delta and marine terraces indicates that uplift of the Amphithea fault block ensued after the emplacement of the slide sheets (Gawthorpe, Andrews, et al., 2017; Gawthorpe, Leeder, et al., 2017). However, it is highly probable that the tilting of the Amphithea hangingwall and triggering of the slide sheets represent an early manifestation of this uplifting process.

8.2 | Structural controls on basin-floor gradients

Changes in bathymetry due to evolving structures are known to affect the deposition of deep-water sedimentary systems (e.g. Ge, Nemeč, Gawthorpe, & Hansen, 2017; Ge, Nemeč, Gawthorpe, Rotevatn, & Hansen, 2018; Gee & Gawthorpe, 2006; Haughton, 2000; Hodgson & Haughton, 2004; Kane et al., 2010; Maier et al., 2017, 2018; Oluboyo et al., 2014). In this study, the subaqueous flows derived from the Mavro delta followed regional, basin-scale, gradients and in their path along the Amphithea fault block were forced to interact with more local structural features such as the presence of internal faults, a tilted hangingwall and monocline flexures on top of growing faults, which in turn, affected their transport and deposition. The RDF in the Amphithea fault block records the interplay between two different fault orientations (Figures 1 and 2a): NE-SW striking faults (internal faults and Koutsa border fault) and NW-SE striking faults (Amphithea and Melissi border faults). Faults of both orientations were active throughout the deposition of the RDF in the study area. Nevertheless, the NE-SW striking faults had a defining control on the orientation of the Mavro-derived sedimentary system below the ~6° angular unconformity, whereas the NW-SE striking faults become the predominant ones after the generation of the ~6° angular unconformity, as observed from the reorientation of the palaeotransport directions across this unconformity (Figures 6b, c and 15).

8.3 | Intrabasinal highs

The presence of the Xylokaastro and Amphithea intrabasinal highs played a fundamental role in funnelling the subaqueous flows from the Mavro delta into the Amphithea hangingwall as well as sourcing the conglomerate-dominated lobes (units 2, 4, 5, 6, 9, 12 and 15). In the case of the Amphithea high it also functioned as a barrier from material sourced from the south, as the compositional analysis of the RDF shows lack of the low grade metamorphic clasts that characterize the Kefalari delta located along the southern margin of the fault block south of the Amphithea high (Figures 1 and 5).

8.4 | Fault block uplift

Sediment fairways in rift basins have a limited lifetime due to the dynamics of the fault networks that define them. Processes such as fault block uplift and subsidence and migration of fault activity are thus responsible for changes in the physiography of the basin, leading to new sediment transport pathways and destruction or enhancement of previous ones (e.g. Gawthorpe & Leeder, 2000; Leeder & Gawthorpe, 1987; Ravnås & Steel, 1998). The Amphithea fault block is an example of a depocentre that evolved from being an effective transport pathway for sediment sourced from the Mavro delta to being an area dominated by gravitational sliding from its southern margin due to fault activity. Ultimately, uplift of the Amphithea fault block occurred, signalling its demise as a depocentre and leading to its subaerial exposure and incision (Gawthorpe, Andrews, et al., 2017; Gawthorpe, Leeder, et al., 2017). The passage from subsidence to uplift in the area reflects the northward migration of the fault activity and concurrent uplift of the southern fault blocks that is observed throughout the Corinth Rift (e.g. Bentham et al., 1991; Ford et al., 2013; Gawthorpe, Leeder, et al., 2017; Leeder et al., 2005; Rohais et al., 2007). During deposition of most of the RDF in the Amphithea fault block the coastline was situated towards the southern margin of the basin, forming a large embayment from the Kefalari and Trikala faults towards the Mavro delta (Figures 1 and 15; Gawthorpe, Leeder, et al., 2017). As faulting migrated northwards, the activity of the Amphithea fault increased, leading to further uplift of the Amphithea high, renewed tilting of the Amphithea hangingwall and triggering of large-scale gravitational sliding in the depocentre. Further migration of fault activity shifted the subsiding areas towards the present day Gulf of Corinth and uplifted southern fault blocks such as the Amphithea depocentre (e.g. Ford et al., 2013; Gawthorpe, Leeder, et al., 2017; Rohais et al., 2007). This processes of fault migration and uplift of the fault blocks in rift basins may lead to the complete erosion of the most proximal early syn-rift successions in more mature basins such as the Red Sea, North Sea and the Atlantic margin (e.g. Steckler et al., 1988; Nøttvedt et al., 2000; Ravnås et al., 2000; Bosworth et al., 2005; Torsvik et al., 2009; Moulin et al., 2010). Hence, the implications of this study provide important insights into the evolution of early syn-rift deep-water successions that are seldom preserved on the rift shoulders.

9 | CONCLUSIONS

Different stages of hangingwall tilt at both large- and local scale and the interaction between them are primary controls on the evolution of the deep-water environment in rift basins,

determining the orientation of the depositional systems, their depositional style and stacking patterns. Studies of clast composition coupled with the analysis of palaeotransport directions are fundamental for a correct assessment of the subaqueous drainage patterns, especially in the recognition of transverse and axial drainage and identification of different sediment sources. The RDF in the Amphithea fault block represents deposition of a subaqueous, deep-water axial transport system sourced from the Mavro delta and, to a much smaller degree, by local intrabasinal sources (Xylokastró and Amphithea highs). Deformation of the hangingwall determined changes in the orientation of the depositional systems due to a combination of the large-scale tilt of the fault block by its border faults and the activity of the smaller faults internal to the depocentre. The structural evolution of the Amphithea fault block shows the interaction between active structures of two different orientations: NE-SW (internal faults and Koutsá border fault) and NW-SE (Amphithea and Melissi border faults). The end of the Amphithea fault block as a deep-water depocentre is marked by the development of large-scale sliding originated from the steepening of its tilted hangingwall and it is interpreted to represent an early symptom of fault block uplift in the area.

Our findings have implications for deep-water rift basin studies in general. The existence of two or more fault orientations influencing the hangingwall gradients is a problem usually tackled from a structural geology perspective (e.g. Henza, Withjack, & Schlische, 2010; Henza, Withjack, & Schlische, 2011; Morley et al., 2004), and ignored in most sedimentary models for deep-water environments (e.g. Gawthorpe & Leeder, 2000; Henstra et al., 2016; Leppard & Gawthorpe, 2006; Ravnås & Steel, 1997; Zhang & Scholz, 2015). This aspect needs better documentation in order to understand the timing of deformation and its control on deep-water systems. Correct identification and mapping of intrabasinal highs is also crucial in attributing different sediment sources and barriers to axial and transverse subaqueous drainage in rift basins.

ACKNOWLEDGEMENTS

This contribution forms part of the Syn-Rift Systems Project funded by the Research Council of Norway, Aker BP, ConocoPhillips, DNO, Equinor, Neptune and Tullow Oil (project number 255229) to the University of Bergen and academic partners the universities of Leeds, East Anglia, Lorraine and the National and Kapodistrian University of Athens. The authors' thank the Segas family for help and support while undertaking fieldwork in the Corinth rift. Reviews by Oliver B. Duffy, Jonathan Obrist-Farner, Benzong Xian and an anonymous reviewer and editorial steering by Cari Johnson are acknowledged. The authors have no conflict of interest to declare.

ORCID

Martin Muravchik  <https://orcid.org/0000-0002-1330-0673>

Rob L. Gawthorpe  <https://orcid.org/0000-0002-4352-6366>

Haralambos Kranis  <https://orcid.org/0000-0002-3626-7300>

REFERENCES

- Armitage, D. A., McHargue, T., Fildani, A., & Graham, S. A. (2012). Postavulsion channel evolution: Niger delta continental slope. *AAPG Bulletin*, *96*, 823–843. <https://doi.org/10.1306/09131110189>
- Azpiroz-Zabala, M., Cartigny, M. J. B., Talling, P. J., Parsons, D. R., Sumner, E. J., Clare, M. A., ... Pope, E. L. (2017). Newly recognized turbidity current structure can explain prolonged flushing of submarine canyons. *Science Advances*, *3*, e1700200. <https://doi.org/10.1126/sciadv.1700200>
- Bentham, P., Collier, R. E. L., Gawthorpe, R. L., Leeder, M. R., Prossor, S., & Stark, C. (1991). Tectono-sedimentary development of an extensional Basin: The neogene megara basin, Greece. *Journal of the Geological Society*, *148*, 923–934. <https://doi.org/10.1144/gsjgs.148.5.0923>
- Bornovas, J., Lalechos, N., Filippakis, N., Christodoulou, G., & Tsaila-Monopoli, S. (1972). *Geological map of Greece: 1:50,000*. Nemea Sheet: IGME Publications, Athens, Greece.
- Bosworth, W., Huchon, P., & McClay, K. R. (2005). The red sea and gulf of aden basins. *Journal of African Earth Sciences*, *43*, 334–378. <https://doi.org/10.1016/j.jafrearsci.2005.07.020>
- Brooks, H. L., Hodgson, D. M., Brunt, R. L., Peakall, J., Hofstra, M., & Flint, S. S. (2018). Deep-water channel-lobe transition zone dynamics: processes and depositional architecture, an example from the karoo basin, South Africa. *Geological Society of America Bulletin*, *130*, 1723–1746. <https://doi.org/10.1130/B31714.1>
- Bull, S., Cartwright, J., & Huuse, M. (2009). A review of kinematic indicators from mass-transport complexes using 3d seismic data. *Marine and Petroleum Geology*, *26*, 1132–1151. <https://doi.org/10.1016/j.marpetgeo.2008.09.011>
- Carvajal, C., Paull, C. K., Caress, D. W., Fildani, A., Lundsten, E., Anderson, K., ... Herguera, J. C. (2017). Unraveling the channel-lobe transition zone with high-resolution AUV bathymetry: Navy fan, offshore Baja California, Mexico. *Journal of Sedimentary Research*, *87*, 1049–1059. <https://doi.org/10.2110/jsr.2017.58>
- Clark, J. D., & Pickering, K. T. (1996). Architectural elements and growth patterns of submarine channels: Application to hydrocarbon exploration. *AAPG Bulletin*, *80*, 194–221.
- Collier, R. E. L., & Dart, C. J. (1991). Neogene to quaternary rifting, sedimentation and uplift in the Corinth Basin, Greece. *Journal of the Geological Society, London*, *148*, 1049–1065. <https://doi.org/10.1144/gsjgs.148.6.1049>
- Cowie, P. A., Gupta, S., & Dawers, N. H. (2000). Implications of Fault Array Evolution for Synrift Depocentre Development: Insights from a Numerical Fault Growth Model. *Basin Research*, *12*, 241–261. <https://doi.org/10.1046/j.1365-2117.2000.00126.x>
- Dasgupta, P. (2003). Sediment gravity flow - the conceptual problems. *Earth-Science Reviews*, *62*, 265–281. [https://doi.org/10.1016/S0012-8252\(02\)00160-5](https://doi.org/10.1016/S0012-8252(02)00160-5)
- Deptuck, M. E., Sylvester, Z., Pirmez, C., & O'Byrne, C. (2007). Migration-aggradation history and 3-D seismic geomorphology of submarine channels in the pleistocene benin-major canyon, western niger delta slope. *Marine and Petroleum Geology*, *24*, 406–433. <https://doi.org/10.1016/j.marpetgeo.2007.01.005>
- di Celma, C. N., Brunt, R. L., Hodgson, D. M., Flint, S. S., & Kavanagh, J. P. (2011). Spatial and temporal evolution of a permian submarine slope channel-levee system, karoo basin, South Africa. *Journal of Sedimentary Research*, *81*, 579–599. <https://doi.org/10.2110/jsr.2011.49>
- Fabuel-Pérez, I., Hodgetts, D., & Redfern, J. (2009). A new approach for outcrop characterization and geostatistical analysis of a low-sinuosity fluvial-dominated succession using digital outcrop models: Upper Triassic Oukaimeden Sandstone Formation, Central High Atlas, Morocco. *AAPG Bulletin*, *93*, 795–827. <https://doi.org/10.1306/02230908102>
- Ferentinos, G., Papatheodorou, G., & Collins, M. B. (1988). Sediment transport processes on an active submarine fault escarpment: Gulf of Corinth, Greece. *Marine Geology*, *83*, 43–61. [https://doi.org/10.1016/0025-3227\(88\)90051-5](https://doi.org/10.1016/0025-3227(88)90051-5)
- Fildani, A., Hubbard, S. M., Covault, J. A., Maier, K. L., Romans, B. W., Traer, M., & Rowland, J. C. (2013). Erosion at inception of deep-sea channels. *Marine and Petroleum Geology*, *41*, 48–61. <https://doi.org/10.1016/j.marpetgeo.2012.03.006>
- Ford, M., Rohais, S., Williams, E. A., Bourlange, S., Jousselin, D., Backert, N., & Malartre, F. (2013). Tectono-sedimentary evolution of the western corinth rift (Central Greece). *Basin Research*, *25*, 3–25. <https://doi.org/10.1111/j.1365-2117.2012.00550.x>
- Frey Martinez, J., Cartwright, J., & Hall, B. (2005). 3d seismic interpretation of slump complexes: Examples from the continental margin of Israel. *Basin Research*, *17*, 83–108. <https://doi.org/10.1111/j.1365-2117.2005.00255.x>
- Frey-Martínez, J., Cartwright, J., & James, D. (2006). Frontally confined versus frontally emergent submarine landslides: A 3d seismic characterisation. *Marine and Petroleum Geology*, *23*, 585–604. <https://doi.org/10.1016/j.marpetgeo.2006.04.002>
- Gawthorpe, R. L., Andrews, J. E., Collier, R. E. L., Ford, M., Henstra, G. A., Kranis, H., ... Skourtsos, E. (2017). Building up or Out? disparate sequence architectures along an active rift margin—corinth rift, Greece. *Geology*, *45*, 1111–1114. <https://doi.org/10.1130/G39660.1>
- Gawthorpe, R. L., & Leeder, M. R. (2000). Tectono-sedimentary evolution of active extensional basins. *Basin Research*, *12*, 195–218. <https://doi.org/10.1046/j.1365-2117.2000.00121.x>
- Gawthorpe, R. L., Leeder, M. R., Kranis, H., Skourtsos, E., Andrews, J. E., Henstra, G. A., ... Stamatakis, M. (2017). Tectono-sedimentary evolution of the Plio-Pleistocene Corinth rift, Greece. *Basin Research*, *30*, 448–479. <https://doi.org/10.1111/bre.12260>
- Ge, Z., Nemeč, W., Gawthorpe, R. L., & Hansen, E. W. M. (2017). Response of unconfined turbidity current to normal-fault topography. *Sedimentology*, *64*, 932–959. <https://doi.org/10.1111/sed.12333>
- Ge, Z., Nemeč, W., Gawthorpe, R. L., Rotevatn, A., & Hansen, E. W. M. (2018). Response of unconfined turbidity current to relay-ramp topography: insights from process-based numerical modelling. *Basin Research*, *30*, 321–343. <https://doi.org/10.1111/bre.12255>
- Gee, M. J. R., & Gawthorpe, R. L. (2006). Submarine channels controlled by salt tectonics: Examples from 3d seismic data offshore angola. *Marine and Petroleum Geology*, *23*, 443–458. <https://doi.org/10.1016/j.marpetgeo.2006.01.002>
- Gee, M. J. R., Gawthorpe, R. L., Bakke, K., & Friedmann, S. J. (2007). Seismic geomorphology and evolution of submarine channels from

- the angolan continental margin. *Journal of Sedimentary Research*, 77, 433–446. <https://doi.org/10.2110/jsr.2007.042>
- Haughton, P. D. W. (2000). Evolving turbidite systems on a deforming basin floor, tabernas, Se Spain. *Sedimentology*, 47, 497–518. <https://doi.org/10.1046/j.1365-3091.2000.00293.x>
- Henstra, G. A., Grundvåg, S.-A., Johannessen, E. P., Kristensen, T. B., Midtkandal, I., Nystuen, J. P., ... Windelstad, J. (2016). Depositional processes and stratigraphic architecture within a coarse-grained rift-margin turbidite system: The wollaston forland group, east Greenland. *Marine and Petroleum Geology*, 76, 187–209. <https://doi.org/10.1016/j.marpetgeo.2016.05.018>
- Henza, A. A., Withjack, M. O., & Schlische, R. W. (2010). Normal-fault development during two phases of non-coaxial extension: An experimental study. *Journal of Structural Geology*, 32, 1656–1667. <https://doi.org/10.1016/j.jsg.2009.07.007>
- Henza, A. A., Withjack, M. O., & Schlische, R. W. (2011). How do the properties of a pre-existing normal-fault population influence fault development during a subsequent phase of extension? *Journal of Structural Geology*, 33, 1312–1324. <https://doi.org/10.1016/j.jsg.2011.06.010>
- Hodgetts, D. (2009). LiDAR in the environmental sciences: Geological applications. In G. Heritage, & A. Large (Eds.), *Laser scanning for the environmental sciences* (pp. 165–179). Oxford: Wiley-Blackwell.
- Hodgson, D. M., Flint, S. S., Hodgetts, D., Drinkwater, N. J., Johannessen, E. P., & Luthi, S. M. (2006). Stratigraphic evolution of fine-grained submarine fan systems, Tanqua Depocenter, Karoo Basin, South Africa. *Journal of Sedimentary Research*, 76, 20–40. <https://doi.org/10.2110/jsr.2006.03>
- Hodgson, D. M., & Haughton, P. D. W. (2004). Impact of syndepositional faulting on gravity current behaviour and deep-water stratigraphy: Tabernas-sorbas Basin, Se Spain. In: S. A. Lomas & P. Joseph (Eds.), *Confined turbidite systems* (pp. 135–158), Geological Society, London, Special Publications, 222.
- Hubbard, S. M., Covault, J. A., Fildani, A., & Romans, B. W. (2014). Sediment transfer and deposition in slope channels: Deciphering the record of enigmatic deep-sea processes from outcrop. *Geological Society of America Bulletin*, 126, 857–871. <https://doi.org/10.1130/B30996.1>
- Hubbard, S. M., Romans, B. W., & Graham, S. A. (2008). Deep-water foreland basin deposits of the cerro Toro formation, Magallanes Basin, Chile: Architectural elements of a sinuous basin axial channel belt. *Sedimentology*, 55, 1333–1359. <https://doi.org/10.1111/j.1365-3091.2007.00948.x>
- Jackson, C. A. L., Larsen, E., Hanslien, S., & Tjemsland, A. E. (2011). Controls on Synrift turbidite deposition on the hanging wall of the south Viking graben, North Sea rift system, offshore Norway. *AAPG Bulletin*, 95, 1557–1587. <https://doi.org/10.1306/01031110037>
- Janocko, M., Nemeč, W., Henriksen, S., & Warchoń, M. (2013). The diversity of deep-water sinuous channel belts and slope valley-fill complexes. *Marine and Petroleum Geology*, 41, 7–34. <https://doi.org/10.1016/j.marpetgeo.2012.06.012>
- Johnson, S. D., Flint, S. S., Hinds, D., & de Ville Wickens, H., (2001). Anatomy, geometry and sequence stratigraphy of basin floor to slope turbidite systems, Tanqua Karoo, South Africa. *Sedimentology*, 48, 987–1023. <https://doi.org/10.1046/j.1365-3091.2001.00405.x>
- Kane, I. A., Catterall, V., McCaffrey, W. D., & Martinsen, O. J. (2010). Submarine channel response to Intrabasinal Tectonics: The influence of lateral tilt. *AAPG Bulletin*, 94, 189–219. <https://doi.org/10.1306/08180909059>
- Kneller, B. C., & Branney, M. J. (1995). Sustained high-density turbidity currents and deposition of thick massive sands. *Sedimentology*, 42, 607–616.
- Koutsouveli, A., Mettos, A., Tsapralis, V., Tsaila-Monopoli, S., & Ioakim, C. (1989). *Geological map of Greece: 1:50,000*. Xylokastró Sheet: IGME Publications, Athens, Greece.
- Leeder, M. R., Collier, R. E. L., Abdul Aziz, L. H., Trout, M., Ferentinis, G., Papatheodorou, G., & Lyberis, E. (2002). Tectono-sedimentary processes along an active marine/lacustrine half-graben margin: Alkyonides Gulf, E. Gulf of Corinth. *Greece. Basin Research*, 14, 25–41. <https://doi.org/10.1046/j.1365-2117.2002.00164.x>
- Leeder, M. R., & Gawthorpe, R. L. (1987). Sedimentary models for extensional tilt-block/half-graben basins. In: M. P. Coward, J. F. Dewey, & P. L. Hancock (Eds.), *Continental Extensional Tectonics* (pp. 139–152), Geological Society, London, Special Publications, Vol. 28.
- Leeder, M. R., Mack, G. H., Brasier, A. T., Parrish, R. R., McIntosh, W. C., Andrews, J. E., & Duermeijer, C. E. (2008). Late-pliocene timing of corinth (Greece) rift-margin fault migration. *Earth and Planetary Science Letters*, 274, 132–141. <https://doi.org/10.1016/j.epsl.2008.07.006>
- Leeder, M. R., Mark, D. F., Gawthorpe, R. L., Kranis, H., Loveless, S., Pedentchouk, N., ... Stamatakis, M. (2012). A "Great Deepening": Chronology of Rift Climax, Corinth Rift, Greece. *Geology*, 40, 999–1002. <https://doi.org/10.1130/G33360.1>
- Leeder, M. R., Portman, C., Andrews, J. E., Collier, R. E. L., Finch, E., Gawthorpe, R. L., ... Rowe, P. J. (2005). Normal faulting and crustal deformation, Alkyonides Gulf and perachora peninsula, eastern gulf of corinth rift, Greece. *Journal of the Geological Society, London*, 162, 549–561. <https://doi.org/10.1144/0016-764904-075>
- Leppard, C. W., & Gawthorpe, R. L. (2006). Sedimentology of rift climax deep water systems; Lower rudeis formation, hammam faraun fault block, Suez Rift. *Egypt. Sedimentary Geology*, 191, 67–87. <https://doi.org/10.1016/j.sedgeo.2006.01.006>
- Lewis, K. B. (1971). Slumping on a continental slope inclined at 1°–4°. *Sedimentology*, 16, 97–110.
- Li, P., Kneller, B. C., Hansen, L., & Kane, I. A. (2016). The classical turbidite outcrop at san clemente, California Revisited: An example of sandy submarine channels with asymmetric facies architecture. *Sedimentary Geology*, 346, 1–16. <https://doi.org/10.1016/j.sedgeo.2016.10.001>
- Lucente, C. C., & Pini, G. A. (2003). Anatomy and emplacement mechanism of a large submarine slide within a Miocene Foredeep in the Northern Apennines, Italy: A field perspective. *American Journal of Science*, 303, 565–602. <https://doi.org/10.2475/ajs.303.7.565>
- Maier, K. L., Brothers, D. S., Paull, C. K., McGann, M., Caress, D. W., & Conrad, J. E. (2017). Records of continental slope sediment flow morphodynamic responses to gradient and active faulting from integrated Auv and Rov Data, Offshore Palos Verdes, Southern California Borderland. *Marine Geology*, 393, 47–66. <https://doi.org/10.1016/j.marpetgeo.2016.10.001>
- Maier, K. L., Roland, E. C., Walton, M. A. L., Conrad, J. E., Brothers, D. S., Dartnell, P., & Kluesner, J. W. (2018). The tectonically controlled san gabriel channel-lobe transition zone, Catalina Basin, Southern California Borderland. *Journal of Sedimentary Research*, 88, 942–959. <https://doi.org/10.2110/jsr.2018.50>
- McArthur, A. D., Kneller, B. C., Wakefield, M. I., Souza, P. A., & Kuchle, J. (2016). Palynofacies classification of the depositional elements of confined turbidite systems: examples from the Gres D'annot, Se France. *Marine and Petroleum Geology*, 77, 1254–1273. <https://doi.org/10.1016/j.marpetgeo.2016.08.020>

- Moernaut, J., & de Batist, M. (2011). Frontal emplacement and mobility of sublacustrine landslides: Results from morphometric and seismostratigraphic analysis. *Marine Geology*, 285, 29–45. <https://doi.org/10.1016/j.margeo.2011.05.001>
- Morley, C. K., Haranya, C., Phoosongsee, W., Pongwapee, S., Kornsawan, A., & Wanganan, N. (2004). Activation of rift oblique and rift parallel pre-existing fabrics during extension and their effect on deformation style: Examples from the rifts of Thailand. *Journal of Structural Geology*, 26, 1803–1829. <https://doi.org/10.1016/j.jsg.2004.02.014>
- Morris, E. A., Hodgson, D. M., Brunt, R. L., & Flint, S. S. (2014). Origin, evolution and anatomy of silt-prone submarine external levées. *Sedimentology*, 61, 1734–1763. <https://doi.org/10.1111/sed.12114>
- Moulin, M., Aslanian, D., & Unternehr, P. (2010). A new starting point for the South and Equatorial Atlantic Ocean. *Earth-Science Reviews*, 98, 1–37. <https://doi.org/10.1016/j.earscirev.2009.08.001>
- Muravchik, M., Bilmes, A., D'Elia, L., & Franzese, J. R. (2014). Alluvial fan deposition along a rift depocentre border from the neuquén basin, Argentina. *Sedimentary Geology*, 301, 70–89. <https://doi.org/10.1016/j.sedgeo.2013.12.007>
- Muravchik, M., Gawthorpe, R. L., Sharp, I. R., Rarity, F., & Hodgetts, D. (2018). Sedimentary environment evolution in a marine hanging-wall dip slope setting. El Qaa Fault Block, Suez Rift. *Egypt. Basin Research*, 30, 452–478. <https://doi.org/10.1111/bre.12231>
- Normark, W. R. (1978). Fan valleys, channels, and depositional lobes on modern submarine fans: Characters for recognition of sandy turbidite environments. *AAPG Bulletin*, 62, 912–931.
- Normark, W. R., Piper, D. J. W., & Hess, G. R. (1979). Distributary channels, sand lobes, and mesotopography of navy submarine fan, California borderland, with applications to ancient fan sediments. *Sedimentology*, 26, 749–774. <https://doi.org/10.1111/j.1365-3091.1979.tb00971.x>
- Nøttvedt, A., Berge, A. M., Dawers, N. H., Færseth, R. B., Häger, K. O., Mangerud, G., & Puigdefabregas, C. (2000). Syn-rift evolution and resulting play models in the Snorre-H area, northern North Sea. *Geological Society, London, Special Publications*, 167, 179–218.
- Oluboyo, A. P., Gawthorpe, R. L., Bakke, K., & Hadler-Jacobsen, F. (2014). Salt tectonic controls on deep-water turbidite depositional systems: Miocene, southwestern Lower Congo Basin, offshore Angola. *Basin Research*, 26, 597–620. <https://doi.org/10.1111/bre.12051>
- Papatheodorou, G., & Ferentinos, G. (1993). Sedimentation processes and basin-filling depositional architecture in an active asymmetric graben: Strava graben, Gulf of Corinth, Greece. *Basin Research*, 5, 235–253. <https://doi.org/10.1111/j.1365-2117.1993.tb00069.x>
- Pemberton, E. A. L., Hubbard, S. M., Fildani, A., Romans, B., & Stright, L. (2016). The stratigraphic expression of decreasing confinement along a deep-water sediment routing system: Outcrop example from southern Chile. *Geosphere*, 12, 114–134. <https://doi.org/10.1130/GES01233.1>
- Pe-Piper, G., & Koukouvelas, I. (1990). Petrology and geochemistry of granitic pebbles in the pliocene fluvial deposits of the north-west peloponnesse (Greece) and their regional significance. *Neues Jahrbuch Für Mineralogie - Abhandlungen*, 161, 327–343.
- Pe-Piper, G., & Koukouvelas, I. (1992). Petrology, geochemistry and regional significance of igneous clasts pebbles in parnassos flysch, amphissa area, greece. *Neues Jahrbuch Für Mineralogie - Abhandlungen*, 164, 94–112.
- Pe-Piper, G., & Piper, D. J. W. (1991). Early mesozoic oceanic subduction-related volcanic rocks, Pindos Basin, Greece. *Tectonophysics*, 192, 273–292. [https://doi.org/10.1016/0040-1951\(91\)90104-Z](https://doi.org/10.1016/0040-1951(91)90104-Z)
- Posamentier, H. W., & Kolla, V. (2003). Seismic geomorphology and stratigraphy of depositional elements in deep-water settings. *Journal of Sedimentary Research*, 73, 367–388. <https://doi.org/10.1306/111302730367>
- Prélat, A., & Hodgson, D. M. (2013). The Full Range of Turbidite Bed Thickness Patterns in Submarine Lobes: Controls and Implications. *Journal of the Geological Society*, 170, 209–214. <https://doi.org/10.1144/jgs2012-056>
- Prélat, A., Hodgson, D. M., & Flint, S. S. (2009). Evolution, architecture and hierarchy of distributary deep-water deposits: a high-resolution outcrop investigation from the Permian Karoo Basin, South Africa. *Sedimentology*, 56, 2132–2154. <https://doi.org/10.1111/j.1365-3091.2009.01073.x>
- Rarity, F., van Lanen, X. M. T., Hodgetts, D., Gawthorpe, R. L., Wilson, P., Fabuel-Pérez, I., & Redfern, J. (2014). Lidar-Based Digital Outcrops for Sedimentological Analysis: Workflows and Techniques. In: A. W. Martinius, J. A. Howell, & T. R. Good (Eds.), *Sediment-Body Geometry and Heterogeneity: Analogue Studies for Modelling the Subsurface* (pp. 153–183), Geological Society, London, Special Publications, Vol. 387.
- Ravnås, R., Nøttvedt, A., Steel, R. J., & Windelstad, J. (2000). Syn-rift sedimentary architectures in the Northern North Sea. In: A. Nøttvedt (Ed.), *Dynamics of the Norwegian Margin*, Geological Society, London, Special Publication, Vol. 167, 133–177.
- Ravnås, R., & Steel, R. J. (1997). Contrasting styles of late jurassic syn-rift turbidite sedimentation: A comparative study of the magnus and oseberg areas, Northern North Sea. *Marine and Petroleum Geology*, 14, 417–449. [https://doi.org/10.1016/S0264-8172\(97\)00010-X](https://doi.org/10.1016/S0264-8172(97)00010-X)
- Ravnås, R., & Steel, R. J. (1998). Architecture of marine rift-basin successions. *AAPG Bulletin*, 82, 110–146.
- Rohais, S., Eschard, R., Ford, M., Guillocheau, F., & Moretti, I. (2007). Stratigraphic architecture of the plio-pleistocene infill of the corinth rift: implications for its structural evolution. *Tectonophysics*, 440, 5–28. <https://doi.org/10.1016/j.tecto.2006.11.006>
- Skourtsos, E., Kranis, H., Zambetakis-Lekkas, A., Gawthorpe, R. L., & Leeder, M. (2016). Alpine basement outcrops at northern peloponnesus: implications for the early stages in the evolution of the corinth rift. *Bulletin of the Geological Society of Greece*, 50, 153–163. <https://doi.org/10.12681/bgsg.11714>
- Smith, D. P., & Busby, C. J. (1993). Mid-Cretaceous crustal extension recorded in deep-marine half-graben fill, Cedros Island, Mexico. *Geological Society of America Bulletin*, 105, 547–562. [https://doi.org/10.1130/0016-7606\(1993\)105<0547:MCCERI>2.3.CO;2](https://doi.org/10.1130/0016-7606(1993)105<0547:MCCERI>2.3.CO;2)
- Sohn, Y. K. (2000). Depositional processes of submarine debris flows in the Miocene fan deltas, pohang basin, se korea with special reference to flow transformation. *Journal of Sedimentary Research*, 70, 491–503. <https://doi.org/10.1306/2DC40922-0E47-11D7-8643000102C1865D>
- Sohn, Y. K., Kim, S. B., Hwang, I. G., Bahk, J. J., Choe, M. Y., & Chough, S. K. (1997). Characteristics and depositional processes of large-scale gravelly gilbert-type foresets on the Miocene doomsan fan delta, pohang basin, Se Korea. *Journal of Sedimentary Research*, 67, 130–141.
- Spychala, Y. T., Hodgson, D. M., Stevenson, C. J., & Flint, S. S. (2017). Aggradational lobe fringes: The influence of subtle intrabasinal seabed topography on sediment gravity flow processes and

- lobe stacking patterns. *Sedimentology*, *64*, 582–608. <https://doi.org/10.1111/sed.12315>
- Steckler, M. S., Berthelot, F., Lyberis, N., & le Pichon, X. (1988). Subsidence in the gulf of suez: implications for rifting and plate kinematics. *Tectonophysics*, *153*, 249–270. [https://doi.org/10.1016/0040-1951\(88\)90019-4](https://doi.org/10.1016/0040-1951(88)90019-4)
- Stevenson, C. J., Jackson, C. A. L., Hodgson, D. M., Hubbard, S. M., & Eggenhuisen, J. T. (2015). Deep-water sediment bypass. *Journal of Sedimentary Research*, *85*, 1058–1081. <https://doi.org/10.2110/jsr.2015.63>
- Strachan, L. J., Rarity, F., Gawthorpe, R. L., Wilson, P., Sharp, I. R., & Hodgetts, D. (2013). Submarine slope processes in rift-margin basins, Miocene Suez Rift. *Egypt. Geological Society of America Bulletin*, *125*, 109–127. <https://doi.org/10.1130/B30665.1>
- Sumner, E. J., Talling, P. J., Amy, L. A., Wynn, R. B., Stevenson, C. J., & Frenz, M. (2012). Facies architecture of individual basin-plain turbidites: comparison with existing models and implications for flow processes. *Sedimentology*, *59*, 1850–1887. <https://doi.org/10.1111/j.1365-3091.2012.01329.x>
- Symons, W. O., Sumner, E. J., Paull, C. K., Cartigny, M. J. B., Xu, J. P., Maier, K. L., ... Talling, P. J. (2017). A new model for turbidity current behavior based on integration of flow monitoring and precision coring in a submarine canyon. *Geology*, *45*, 367–370. <https://doi.org/10.1130/G38764.1>
- Talling, P. J., Masson, D. G., Sumner, E. J., & Malgesini, G. (2012). Subaqueous sediment density flows: depositional processes and deposit types. *Sedimentology*, *59*, 1937–2003. <https://doi.org/10.1111/j.1365-3091.2012.01353.x>
- Tataris, A., Maragoudakis, N., Kounis, G., Christodoulou, G., & Tsaila-Monopoli, S. (1970). *Geological map of Greece: 1:50,000*. Nemea Sheet: IGME Publications, Athens, Greece.
- Torsvik, T. H., Rousse, S., Labails, C., & Smethurst, M. A. (2009). A new scheme for the opening of the South Atlantic Ocean and the dissection of an Aptian salt basin. *Geophysical Journal International*, *177*, 1315–1333. <https://doi.org/10.1111/j.1365-246X.2009.04137.x>
- Tsoflias, P., Fleury, J. J., & Ioakim, C. (1993). *Geological map of Greece: 1:50,000*. Derveni Sheet: IGME Publications, Athens, Greece.
- Winn, R. D., & Dott, R. H. (1979). Deep-water fan-channel conglomerates of late cretaceous age, Southern Chile. *Sedimentology*, *26*, 203–228. <https://doi.org/10.1111/j.1365-3091.1979.tb00351.x>
- Wynn, R. B., Kenyon, N. H., Masson, D. G., Stow, D. A. V., & Weaver, P. P. E. (2002). Characterization and recognition of deep-water channel-lobe transition zones. *AAPG Bulletin*, *86*, 1441–1462.
- Zhang, X., & Scholz, C. A. (2015). Turbidite systems of lacustrine rift basins: Examples from the Lake Kivu and Lake Albert rifts, East Africa. *Sedimentary Geology*, *325*, 177–191. <https://doi.org/10.1016/j.sedgeo.2015.06.003>
- Zhang, X., Scholz, C. A., Hecky, R. E., Wood, D. A., Zal, H. J., & Ebinger, C. J. (2014). Climatic control of the late Quaternary turbidite sedimentology of Lake Kivu, East Africa: Implications for deep mixing and geologic hazards. *Geology*, *42*, 811–814. <https://doi.org/10.1130/G35818.1>
- Ziegler, P. A., & Cloethingh, S. (2004). Dynamic processes controlling evolution of Rifted Basins. *Earth-Science Reviews*, *64*, 1–50. [https://doi.org/10.1016/S0012-8252\(03\)00041-2](https://doi.org/10.1016/S0012-8252(03)00041-2)

SUPPORTING INFORMATION

Additional supporting information may be found online in the Supporting Information section.

Supinfo

How to cite this article: Muravchik M, Henstra GA, Eliassen GT, et al. Deep-water sediment transport patterns and basin floor topography in early rift basins: Plio-Pleistocene syn-rift of the Corinth Rift, Greece. *Basin Res.* 2019;00:1–29. <https://doi.org/10.1111/bre.12423>